Efficient simulation of rarefied gas flow past a particle: A boundary element method for the linearized G13 equations

Juan C. Padrino[1,†,‡], James E. Sprittles[2] and Duncan A. Lockerby[1,†]
[1]School of Engineering, University of Warwick, Coventry CV4 7AL, UK
[2]Mathematics Institute, University of Warwick, Coventry CV4 7AL, UK

May 9, 2022

Abstract

We develop a novel boundary integral formulation for the steady linearized form of Grad's 13-moment (G13) equations applied to uniform flow of rarefied gas past solid objects at low Mach numbers. Changing variables leads to a system of boundary integral equations that combines integral equations from Stokes flow and potential theory. The strong coupling between the stress deviator and heat flux featured by the G13 equations demands adding a boundary integral equation for the pressure. We specialize the integral equations for axisymmetric flow with no swirl and derive the axisymmetric fundamental solutions for the pressure equation, seemingly absent in the Stokes-flow literature. Using the boundary element method to achieve a numerical solution, we apply this formulation to streaming flow of rarefied gas past prolate or oblate spheroids with their axis of symmetry parallel to the free stream, considering various aspect ratios and Knudsen numbers — the ratio of the molecules' mean free path to the macroscopic length scale. After validating the method, we obtain the surface profiles of the deviations from the unperturbed state of the traction, heat flux, pressure, temperature, and slip velocity, as well as the drag on the spheroid, observing convergence with the number of elements. Rarefaction phenomena such as temperature jump and polarization, Knudsen effects in the drag, and velocity slippage are predicted. This method opens a new path for investigating other gas non-equilibrium phenomena that can be modelled by the same set of equations, such as thermophoresis, and has application in nano- and microfluidics.

Key words: low-Reynolds-number flows; micro-/nano-fluid dynamics; rarefied gas flow; spheroid; boundary integral equation; boundary element method.

1 Introduction

1.1 Preliminaries

In nano- or micro-channels, such as the narrow conduits assembled into nano- or micro-electro-mechanical systems (NEMS or MEMS) with cross sections having dimensions in the sub-micron or micron range, respectively, gas motion is likely affected by rarefaction non-equilibrium effects. For instance, gas motion may be driven not only by pressure gradients, but also by temperature gradients along walls, causing, for example, thermal creep from cold to hot regions, a well-known consequence of rarefaction (Karniadakis et al., 2005). Gas rarefaction phenomena may also arise in external flows such as in flow around small aerosol particles or in low-density conditions, such as in vacuum or high-altitude (Luo and Pozrikidis, 2008; Nieto et al., 2012). Already in the nineteenth century, Tyndall (1870) noted the displacement of atmospheric dust away from a heated surface, a rarefied effect now known as thermophoresis, related to thermal creep, and caused by forces acting on the suspended

[†]Email addresses for correspondence: padr0006@umn.edu, duncan.lockerby@warwick.ac.uk.
[‡]Currently at Newcastle University, School of Engineering, Newcastle upon Tyne NE1 7RU, UK.

particles from hot to cold (Sone, 2007). As we will see, comparing the size of the passage containing the gas or of the particle surrounded by it with the mean free path of the gas molecules gives a good indication of how influential these non-equilibrium effects can be.

The focus of the present work is on low-speed external flow of a rarefied gas past objects. Modelling this class of flows has potential application in various important sectors, such as health, atmospheric science, and security, examples being the process of inhalation of fine particulate (Lighty et al., 2000; World Health Organization, 2003) or virus-laden microdroplets (Morawska and Milton, 2020; Wilson et al., 2020), the motion of airborne volcanic ash (Heiken, 1994; Rose et al., 2001; Rose and Durant, 2009; Schwaiger et al., 2012), and the transport of bacteria-carrying aerosolized droplets (Settles, 2006; Corriveau, 2016; see also Kesavan et al., 2016), respectively.

The level of rarefaction of a gas is determined by how far, on average, a molecule has to travel to collide with another in comparison with the characteristic length scale of the flow — the gap size in the case of channels or the particle size (Nguyen and Wereley, 2006; Kandlikar et al., 2014). The ratio of the molecular mean free path to the flow geometry characteristic length scale is typically referred to as the Knudsen number, Kn. When the molecular mean free path is significant relative to the scale of the flow, thermodynamic equilibrium cannot be maintained as the frequency of particle collisions within the gas is not high enough. Deviations from local thermodynamic equilibrium in the flow first occur near the walls, where there are fewer inter-molecular collisions than at its core (Kandlikar et al., 2014). These deviations appear macroscopically as differences in tangential velocity and temperature between the fluid and the solid at the boundaries.

Depending on the range of the Knudsen number, appropriate fluid flow and heat transfer models can be chosen. In terms of Kn, the following flow regimes are commonly accepted (Kandlikar et al., 2014): For $Kn < 10^{-3}$, the flow is continuum, and the compressible Navier-Stokes-Fourier (NSF) equations with the no-slip and continuous temperature boundary conditions can be confidently applied. In the range $10^{-3} < Kn < 0.1$, the flow is a slip flow and the NSF equations are still valid, provided the boundary conditions include velocity slip and temperature jump. For $0.1 < Kn < 10$, the flow is said to be in transition and the NSF equations cease to be valid. Finally, for $Kn > 10$, the regime is labelled as free molecular flow and a method that directly solves the Boltzmann equation, using for instance a particulate method, is needed. Air at sea-level pressure, with a mean free path of about 0.07 μm, moving around suspended particles measuring from 0.1 to 5 μm, exemplifies transitional flow (Lockerby and Collyer, 2016). Although the Boltzmann equation is valid in all flow regimes, the application of particulate methods in the transition region is regarded as computationally costly because, in this regime, the gas density is relatively high and a prohibitively large number of particles are needed in the simulations (Agarwal et al., 2001).

In the slip flow regime, the usual set of boundary conditions, used alongside the NSF equations, are the Maxwell velocity slip model, given by the sum of a term proportional to the tangential stress and a term proportional to the tangential component of the temperature gradient, and the Smoluchowski model for the temperature jump, given by a term proportional to the normal component of the temperature gradient (Karniadakis et al., 2005). These constraints are often termed as the Maxwell-Smoluchowski boundary conditions. For slow gas flow past particles with size in the micro- or nanometer range, the Mach number may be low and the Reynolds number vanishingly small. In these conditions and for steady flow, linearization of the NSF model is justified yielding, in the bulk, the Stokes flow equations together with the Laplace equation for the temperature. If these equations are supplemented with the Maxwell-Smoluchowski boundary conditions, assuming the flow is in the slip regime, and no spatial variations of the temperature are imposed either in the far field or within the particle, the gas flow will remain isothermal, so that the temperature jump boundary condition can be dropped and the velocity slip will be determined solely by the shear stress. Maxwell slip boundary condition then becomes essentially equivalent to the widely used Navier slip model (Navier, 1823).

Stokes flow past a sphere with Navier slip was solved exactly by Bassett (1888). For spheroids that deviate slightly from sphericity, the drag on the particle was computed approximately with perturbative techniques by Senchenko and Keh (2006) and Chang and Keh (2009b), whereas for spheroids of

larger aspect ratios, the problem of the slow flow around an axisymmetric particle translating steadily along its axis of revolution was investigated numerically by Keh and Huang (2004) with a method of internal singularity distributions. Later, Keh and Chang (2008) computed more accurately the approximate drag for this case using a series expansion of semi-separable terms whose coefficients were determined numerically with the collocation method, or analytically with a leading-order asymptotic solution. Numerical investigations of Stokes flow with surface slip have been carried out using boundary integral methods for the motion of a sphere in linear flow with or without a plane wall, and the interception of two spheres by Luo and Pozrikidis (2008) and (2007), respectively, and for the complicated three-dimensional geometry of MEMS by Frangi et al. (2006) and Frangi (2012).

By contrast, when a temperature gradient is imposed in the far-field in a rarefied gas otherwise at a uniform temperature, temperature deviations and fluid motion will potentially be predicted by the steady, linearized NSF equations with the Maxwell-Smoluchowski boundary conditions. In the remainder of the paper, for the sake of compactness, we will refer to this model simply as the 'NSF model with slip and jump'. In this case, for a spheroid of aspect ratio near one, an approximate solution was obtained by Senchenko and Keh (2007) with perturbation techniques and, for a spheroid of arbitrary aspect ratio, by Chang and Keh (2009a) using the singularity-collocation method. Two works for rarefied, confined flows in the plane are worthy of mention. First, Nieto et al. (2012) cast these equations as boundary integrals equations and solved them numerically in the case of motions with imposed temperature differences such as the eccentric Couette flow and the shear-driven cavity flow. Later, Nieto et al. (2014) modified their numerical approach to simulate the cavity problem adding the non-linear convective term to the energy equation. However, in a gas flow with negligible Reynolds number, the Peclet number is also insignificant and the convective term can be safely dropped. On the other hand, exact solutions have been obtained with simplified boundary conditions by Leong (1984), Williams (1986), and Keh and Ou (2004) for a spheroid of arbitrary aspect ratio, after neglecting the temperature jump and considering that the slip is only due to the tangential temperature gradient.

1.2 Extended hydrodynamics models based on the moments method

In the early transition regime, say $Kn < 1$, it is necessary (Karniadakis et al., 2005; Kandlikar et al., 2014) and in the late slip flow regime, say $Kn > 10^{-2}$, desirable and, perhaps, advantageous to apply the conservation equations for a continuum, closed with constitutive relationships for the stress and heat-flux, as well as boundary conditions, having Knudsen-number corrections of some order. It is consistent for these corrections to be such that, when Kn becomes negligible, the NSF equations with classical boundary constraints are recovered. One of such corrected or extended hydrodynamics models is Grad's 13-moment equations (G13). They are derived using the method of moments of Grad (1949), in which the distribution function in the Boltzmann equation is represented as a series of orthogonal Hermite polynomials and the macroscopic variables describing the flow are obtained as moments (integrals) of this distribution. Thirteen moments are needed for the same number of variables, namely, mass density, macroscopic velocity vector, temperature, heat-flux vector, and deviatoric stress tensor (symmetric and trace-free), which typically appear in classical hydrodynamics. The pressure is given by an equation of state, usually the ideal gas law. The method gives rise to constitutive equations for the stress deviator and heat-flux in the form of evolutionary equations containing material derivatives of these quantities coupled with the conservation equations for mass, momentum, and energy. Boundary conditions for the G13 equations, derived in a manner consistent with the bulk equations and describing velocity slip and temperature jumps, are given in Struchtrup (2005b), Young (2011), and, in linearized form, in Lockerby and Collyer (2016). They can also be extracted from Struchtrup et al. (2017) by dropping the higher moments. Although in the transition regime only qualitative trends can be expected, at most, with the G13 equations, they can predict features of the flow of a rarefied gas that the NSF model with slip and jump misses, as we will see below. One disadvantage of the G13 model is its inability to describe Knudsen layers; that is, flow regions adjacent to boundaries where rarefaction is dominant (Young, 2011). Also, Agarwal et al. (2001) mentioned that the G13 moments method gives rise to an entropy equation that violates Gibbs

relation.

The linearized G13 equations were solved by Dwyer (1967) to obtain an expression of the thermophoretic force on a spherical particle predicting, for the first time, the phenomenon of reversed thermophoresis, in which the force points from cold to hot under certain conditions. By formally deriving the boundary conditions for G13, Young (2011) added terms coupling stress with heat flux that were missing in the expressions used by Dwyer. Young then solved the steady, linearized G13 equations for the problems of thermophoresis on a spherical particle driven by a temperature gradient and of uniform gas flow past a sphere. In the case of flow past a sphere, keeping the temperature within the solid and far from it equal and unperturbed, his solution described gas temperature polarization with respect to the plane bisecting the sphere that is perpendicular to the flow. By balancing the thermophoretic force with the drag caused by the flow, the thermophoretic velocity can be predicted. Young chose values of the thermal creep, velocity slip, and temperature jump coefficients based on solutions of the Boltzmann equations from the literature to attain very good agreement with direct results from kinetic theory for the thermophoretic force in the slip regime, predicting also reversed thermophoresis. By contrast, with the classical coefficients that arise from the G13 theory — Young called them Maxwell's values — the force tends to be underpredicted. In addition, by modifying his solution to fit a well-known result for the free-molecular regime, Young improved the predictive capabilities of the model in the transition regime. For $Kn \lesssim 0.2$, he reported that the difference between the large Kn-fitted version of the G13 model for the thermophoretic force and the non-fitted one differ by at most 5%. Recently, it was shown that Young's solution of the G13 equations agreed qualitatively with new experimental data (Bosworth et al., 2016) exhibiting reversed thermophoresis (see Padrino et al., 2019).

Lockerby and Collyer (2016) obtained the fundamental solutions (Green's functions for the entire space) for the steady, linearized G13 equations and applied the method of fundamental solutions to numerically compute the drag caused on a sphere by a uniform flow of a rarefied gas. Whilst the agreement with experiments and kinetic theory is good only for $Kn \lesssim 0.1$, outside this range, in the early transition regime, the difference between the drag from G13 and the reference values is less than the predictions from the NSF theory with slip. Lockerby and Collyer also computed the gas motion around two neighboring solid spheres with uniform but different temperatures. This enabled them to identify the differences and interplay between thermal creep and thermal stress flow.

Another model for rarefied gas dynamics, derived more recently using the moments method, is the regularized 13-moment set of equations (R13), proposed by Struchtrup and Torrilhon (2003). Using the Boltzmann equation as the starting point, these equations are best derived by means of the order of magnitude method (Struchtrup, 2005a; Struchtrup et al., 2017). The R13 equations add higher order terms in Kn than G13 to the constitutive equations for the stress deviator and heat-flux containing gradients of these quantities. Boundary conditions compatible with the R13 equations in the bulk have been derived for boundaries without mass transfer, including walls (Gu and Emerson, 2007; Torrilhon and Struchtrup, 2008), and for evaporating and condensing interfaces (Struchtrup and Frezzotti, 2016; Struchtrup et al., 2017). Unlike G13, this model does partially describe Knudsen layers. When the higher moments are dropped, the R13 equations and corresponding boundary conditions reduce to the G13 model (Struchtrup, 2005b; see also Struchtrup et al., 2017). R13 can give quantitatively accurate results for Kn up to 0.5 (Torrilhon, 2016; Struchtrup et al., 2017) and qualitatively even for Kn in the late transition regime (Torrilhon, 2010). R13 equations have been used to model a variety of canonical flows in the transition regime with low Mach number (see review by Torrilhon, 2016). For instance, for slow flow past a sphere, Torrilhon (2010) predicted temperature polarization when the sphere and the gas in the far field are kept at the same unperturbed temperature. Recently, Claydon et al. (2017) derived the fundamental solutions for the linearized, steady R13 equations.

Because they govern essentially the same familiar macroscopic variables of the classical heat transfer and fluid flow models, by examining the relative importance of the various terms in the G13 or R13 equations, or of other models of extended hydrodynamics for that matter, especially the terms arising from rarefaction, one can gain good physical understanding of the often complicated flow

patterns. This is particularly advantageous if the analytical solution can be obtained. In addition, well established numerical methods of classical hydrodynamics may be readily applied to these equations of rarefied gas dynamics, in contrast to direct solutions of the Boltzmann equation.

When an isothermal unperturbed state is modified by a uniform streaming flow past an object, extended hydrodynamic models, such as G13 and R13, will predict temperature variations (e.g., temperature polarization) in regions neighboring the object because of rarefaction. Besides predicting thermal creep (transpiration), they are also capable of predicting thermal stress flow at the boundaries which, under certain conditions, may become the dominant component of slip flow. In contrast, the NSF model with slip and jump will predict no temperature variation, and the flow remains isothermal. From the modelling perspective, this is a consequence of the models' different levels of coupling between the stress deviator and the heat flux. Extended hydrodynamics models, such as G13 and R13 have a stronger deviatoric stress-heat flux coupling, not only in the bulk equations, via the constitutive relations, but also in the boundary conditions, than the NSF model with slip and jump. In the latter model, the coupling is said to be in one way because it is given by the contribution of the temperature gradient along the boundary to the velocity slip and neither spatial gradients of the heat flux appear in the constitutive equation for the stress deviator nor the other way around.

If an unperturbed state is altered, for instance, by imposing a temperature gradient far from an object, such as in thermophoresis problems, G13 and R13 models will predict temperature variations in the flow, as was the case with the NSF model with slip and jump — although this model is not capable of predicting thermal stress flow. Besides the natural discrepancies in prediction accuracy among the models, a very important difference resulting from the level of stress deviator-heat flux coupling lies in the solution procedure, and is especially consequential if a numerical solver is implemented. Whereas the G13 or R13 equations will have to be solved simultaneously, in general, for the NSF model with slip and jump, the energy equation can be solved first for the temperature and heat flux and then these results can be used next in the solution of the flow field (e.g., see Nieto et al., 2012).

1.3 Scope and objectives

In this work, we present a novel boundary integral formulation for the steady, linearized G13 equations to model the low-speed uniform flow of gas past a solid object in conditions such that rarefaction effects play a role. To write boundary integral equations from partial differential ones, their fundamental solutions are required. Rather than using the fundamental solutions for the steady, linearized G13 equations of Lockerby and Collyer (2016), we show that by introducing two auxiliary fields, namely, a vector and a scalar, given by the linear combination of the dimensionless fluid velocity and heat flux, and of the dimensionless temperature and pressure, respectively, the G13 equations can be written in the form of the Stokes equations for the mass and momentum balances and a Laplace equation for the energy balance. A vector boundary integral equation similar to the velocity-traction equation for Stokes flow but modified to include the heat flux is written by applying a well-known result from the Lorentz reciprocal identity (Lorentz, 1907; Pozrikidis, 1992) and two scalars boundary integral equations for the normal and tangential components of the heat flux are obtained from potential theory. After substituting the temperature boundary condition, the equation for the normal component of the heat flux includes the normal component of the deviatoric stress vector. This is replaced by the normal component of the surface traction plus the pressure to make this equation compatible with the velocity-traction-heat flux boundary integral equation, which involves the traction on the surface of the solid. The appearance of the pressure in the set of boundary integral equations through the temperature boundary condition makes necessary the inclusion of an additional boundary integral equation containing the pressure in order to close the system. This extra equation is provided by a modified version of the boundary integral equation for the pressure in Stokes flow derived by Ladyzhenskaya (1969) (see Kim and Karrila, 2005; also Leal, 2007). Because the velocity-traction boundary integral equation of Stokes flow is known to introduce non-uniqueness of the solution (e.g., Pozrikidis, 1992), following a recommendation from the literature, we include in our set of equations an integral condition for the normal component of the traction on the boundary, which selects the

solution corresponding to zero pressure deviation from the unperturbed state in the far field, provided the flow has a certain kind of fore-aft symmetry.

The set of boundary integral equations for G13 are then reduced for the case of axisymmetric flow with no swirling motion. The performance of the model and numerical scheme is evaluated by applying it to the low-speed streaming flow of a rarefied gas past an ellipsoid of revolution with its axis of symmetry parallel to the free stream. The spherical boundary is investigated as a special case. We solve the set of integral equations numerically using the boundary element method. For a three dimensional problem, the boundary element method requires only the meshing of a surface in the space rather than of a volume. For two-dimensional or axisymmetric problems, it suffices to create a mesh in a curve on the plane instead of in a plane surface. Moreover, boundary conditions at infinity can be included exactly in the boundary integral formulation. The boundary element method thus has the advantage of not requiring a large (artificially truncated) domain with appropriate far field conditions there. On the other hand, and as mentioned before, the method is limited to situations where fundamental solutions exist, such as in the cases of the Stokes flow and Laplace equations.

This is seemingly the first time that the boundary integral method is applied to the G13 equations of rarefied gas dynamics. Even though more accurate results are anticipated from R13 equations than from G13, especially in the early transition regime, we opted as a first step for the G13 model, because of the high complexity, not only of the fundamental solutions for R13, as shown by Claydon et al. (2017), but also of the boundary conditions, which include components, in boundary-fitted coordinates, of third-order tensors — the gradient of the stress. Moreover, with G13, we anticipate obtaining reliable quantitative results in the slip regime and at least qualitatively significant results at the beginning of the transition regime, for Knudsen numbers of the order of 0.1. In the present work, we consider Knudsen numbers up to this order of magnitude.

A salient aspect of the present application is the aforementioned boundary integral equation for the pressure. In the literature on boundary integral methods applied to Stokes flows, without or with slip (Youngren and Acrivos, 1975; Luo and Pozrikidis, 2007, 2008), or with non-equilibrium temperature gradients in the bulk and jumps on the boundary (Nieto et al., 2012), the velocity-traction boundary integral equation is typically the only equation solved, at least on the fluid mechanics side. The pressure equation is only invoked, in a later step, if the surface pressure distribution is sought, which is rarely the case. Therefore, actual applications of Ladyzhenskaya's integral equation for the pressure are very scarce. The first applications were apparently due to Ingber and Li (1991), including the flow past an spheroid formulated in three dimensions, using the pressure equation in a second stage to compute its surface distribution, once the velocity-traction boundary integral equation has been solved for the latter. On the other hand, an application where the pressure equation is essential was treated by Rêgo-Silva et al. (1993) who used it to study pressure gradient-driven three-dimensional flow in ducts with the boundary element method (see also Power and Wrobel, 1995). We are not aware of previous work where the axisymmetric formulation of the pressure boundary integral equation is presented. We therefore derived here the axisymmetric fundamental solutions for this equation needed in the analysis of flows with axial symmetry within the framework of the G13 model. These seemingly new expressions may be useful in fluid dynamics applications of the boundary element method even in situations where rarefaction is insignificant.

Another feature of this work is the simultaneous solution of the boundary integral equations composing the model due to the strong coupling between stress deviator and heat flux in the G13 model. That is, a segregated scheme in which the heat transfer problem is decoupled from the fluid flow one and solved first, such as in the approach by Nieto et al. (2012) with the NSF model with slip and jump, is not possible here. Nevertheless, an alternative to the simultaneous solution scheme might be provided by an iterative procedure, which naturally brings the issue of convergence to the forefront. We do not touch upon this aspect in this article. The interested reader is referred to the work of Ramachandran et al. (2012) for a discussion on iterative methods applied to boundary integral equations for Stokes flow with slip.

This paper is organized as follows. In the next section, we introduce the problem that we will

consider in general terms, and the linearized, steady G13 equations, including the boundary conditions. In Section 3, we cast the partial differential equations of G13 as boundary integral equations, whilst in Section 4, these equations are reduced for the special case of axially symmetric flow without swirl. In Sections 3 and 4, we also introduce and discuss the fore-aft symmetry requirement for the flow and the associated integral constraint on the normal traction component. A numerical solution procedure for these equations is devised in Section 5 by means of the boundary element method, and the various details of the approximation are described. In Section 6, we present and discuss the results of applying the numerical approach to the case of rarefied flow past an ellipsoid of revolution, either prolate or oblate, after validating it with the spherical geometry by comparing with the analytical solution. We then conclude with some final remarks in Section 7.

2 Linearized steady Grad's thirteen-moment equations

Grad's (1949) moment method describes the state of a gas by a set of moments or integrals over the velocity space of products of the phase density, governed by the Boltzmann equation, with polynomials of quantities defined by the molecular velocity. Each of the moments determines a macroscopic quantity. By multiplying the Boltzmann equation with these polynomials and integrating over the velocity space, partial differential equations describing the spatial and temporal change of the macroscopic quantities can be derived. In particular, Grad's thirteen-moment equations (G13) are obtained by choosing the thirteen moments corresponding to the gas density, temperature, the three components of the velocity vector, the three components of the heat flux vector, and the five independent components of the stress deviator tensor, which is symmetric and trace-free. The full non-linear G13 equations and a modern account of their derivation can be found in the textbook by Struchtrup (2005b). For our purposes, it suffices to consider a linearized, steady version of them.

Consider a ground state given by a gas at rest with pressure p_0^*, temperature (in energy units) $\theta_0^* = R^* T_0^*$, where T_0^* is the absolute temperature and R^* is the gas specific constant, and vanishing heat flux and deviatoric stress. Symbol ' * ' is used to denote dimensional quantities. This state of the gas remains unperturbed if we assume that the gas surrounds a rigid body also at rest and having the same temperature as the gas, θ_0^*. Except for the body surface, the gas is unbounded. For modelling purposes, we consider the gas to be monatomic and composed of Maxwell molecules. From the ideal gas law, the gas density is p_0^*/θ_0^* and the viscosity, corresponding to temperature θ_0^*, is μ_0^*. Deviations from the ground state caused, for instance, by perturbing the conditions far from the solid object or by setting it in motion are described by the dimensionless variables pressure p, temperature θ, velocity $\boldsymbol{u}$, heat flux $\boldsymbol{q}$, and deviatoric stress $\boldsymbol{S}$, so that the pressure and temperature of the gas are, respectively, $1+p$ and $1+\theta$. The linearized ideal gas law gives the density deviation, which is thus $p-\theta$. Quantities are nondimensionalized using p_0^* for the pressure and stress deviator, θ_0^* for the temperature, p_0^*/θ_0^* for the density, $\theta_0^{*1/2}$ for the velocity, $p_0^*\theta_0^{*1/2}$ for the heat flux, a characteristic dimension ℓ^* for the length (e.g., the characteristic size of an object), and $p_0^*\,\ell^{*2}$ for a force. The linearized, steady G13 set of equations governing these deviations consists of the following expressions. In the absence of body forces, the mass, momentum, and energy conservation laws are given by

$$\nabla \cdot \boldsymbol{u} = 0, \tag{2.1}$$

$$\nabla p + \nabla \cdot \boldsymbol{S} = 0, \tag{2.2}$$

$$\nabla \cdot \boldsymbol{q} = 0, \tag{2.3}$$

with relations for the stress deviator second-order tensor and heat flux vector defined according to G13 as (Struchtrup, 2005b; Lockerby and Collyer, 2016)

$$\boldsymbol{S} = -2Kn\overline{\nabla \boldsymbol{u}} - \frac{4}{5}Kn\overline{\nabla \boldsymbol{q}}, \tag{2.4}$$

$$\boldsymbol{q} = -\frac{15}{4}Kn\nabla\theta - \frac{3}{2}Kn\nabla \cdot \boldsymbol{S}, \tag{2.5}$$

respectively, also linearized and for a steady flow. The overbar denotes a symmetric and trace-free tensor. We use Kn to denote the Knudsen number, which is computed here from the expression

$$Kn = \frac{\mu_0^* \theta_0^{*1/2}}{p_0^* \ell^*}. \tag{2.6}$$

Note that the molecules' mean free path can be expressed by $(\pi/2)^{1/2}\mu_0^* \theta_0^{*1/2}/p_0^*$ (Maxwell, 1879; Kandlikar et al., 2014); however, in (2.6) we have dropped the order one factor $(\pi/2)^{1/2}$ for convenience. The steady linearized G13 equations comprise expressions (2.1)-(2.5) which should be supplemented with boundary conditions derived in a manner consistent with that of the bulk equations.

By introducing

$$\boldsymbol{w} = \boldsymbol{u} + \frac{2}{5}\boldsymbol{q}, \tag{2.7}$$

we have

$$\boldsymbol{S} = -2Kn\overline{\nabla \boldsymbol{w}}, \tag{2.8}$$

and we may write the momentum conservation as

$$\nabla p - Kn\Delta \boldsymbol{w} = 0, \tag{2.9}$$

with

$$\nabla \cdot \boldsymbol{w} = 0; \tag{2.10}$$

hence, p satisfies Laplace equation (a harmonic function). Moreover, the equation of energy conservation becomes simply

$$\Delta \theta = 0, \tag{2.11}$$

and the heat flux $\boldsymbol{q}$ satisfies the vector Laplace equation. An important consequence of this is that Equation (2.9) can be written as $\nabla p = Kn\Delta \boldsymbol{u}$, that is, the same steady linearized momentum balance of a Newtonian flow (i.e. Stokes flow). Nevertheless, because $\overline{\nabla \boldsymbol{w}} \neq \overline{\nabla \boldsymbol{u}}$, we have, from Equation (2.8), that the flow is not Newtonian. For the purpose of writing a system of boundary integral equations for the G13 model, as we will see, having the equations in terms of $\boldsymbol{w}$, such as in (2.8) and (2.9), rather than $\boldsymbol{u}$ will prove advantageous.

The heat flux $\boldsymbol{q}$ is an irrotational vector field; hence, it can be written as

$$\boldsymbol{q} = \nabla \phi, \tag{2.12}$$

where ϕ is the heat flux potential. After using (2.2) and comparing with (2.5), the heat flux potential is given by

$$\phi = -\frac{15}{4}Kn\,\theta + \frac{3}{2}Kn\,p. \tag{2.13}$$

It thus satisfies

$$\Delta \phi = 0. \tag{2.14}$$

At a gas-solid surface, non-linear boundary conditions for G13 have been derived by Struchtrup (2005b) and also by Young (2011). One condition is a vector equation governing the slippage and another is a scalar equation enforcing a temperature jump. In dimensionless form, these boundary conditions can be written as

$$\boldsymbol{u} = \boldsymbol{u}_w - C_m \frac{2-\chi}{\chi}\sqrt{\frac{\pi}{2}}\boldsymbol{n}\cdot\boldsymbol{S}\cdot(\boldsymbol{1}-\boldsymbol{nn}) - \frac{4}{15}K_{tc}\boldsymbol{q}\cdot(\boldsymbol{1}-\boldsymbol{nn}), \tag{2.15}$$

$$\theta = \theta_w - \frac{1}{4}\boldsymbol{n}\cdot\boldsymbol{S}\cdot\boldsymbol{n} - \frac{4}{15}C_e\frac{2-\chi}{\chi}\sqrt{\frac{\pi}{2}}\boldsymbol{q}\cdot\boldsymbol{n}, \tag{2.16}$$

after linearization. Here, θ_w denotes the temperature deviation from the base state at the surface

on the solid side, and $\boldsymbol{u}_w$ represents the velocity of the solid at its surface; $\boldsymbol{n}$ is the unit vector normal to the gas-solid boundary pointing into the gas; K_{tc}, C_m, and C_e denote the thermal creep, velocity slip, and temperature jump coefficients; symbol χ denotes the accommodation coefficient, which is taken to be the same in both the velocity slip and temperature jump boundary conditions (Struchtrup et al., 2017). As shown by Struchtrup (2005b) and Young (2011), the G13 analysis gives rise to expressions (2.15) and (2.16) with the classical values for the coefficients, namely, $K_{tc} = 3/4$, $C_m = 1$, and $C_e = 15/8$, which Young labeled as Maxwell's values. When the Navier-Stokes-Fourier constitutive relations for the stress deviator and heat-flux are used in the boundary conditions, they reduce to the Maxwell-Smoluchowski slip and jump conditions, with the contribution from the stress deviator to the temperature jump often neglected in the literature (Struchtrup, 2005b). An alternative set of values for these coefficients has been proposed by Young (2011) from accurate solutions of the kinetic equations cited by Sharipov (2004). Whereas results vary significantly with the use of one set of coefficients or the other when a temperature gradient is imposed in the far field — e.g., thermophoresis problem — when a streaming flow is imposed instead, predictions from the G13 model are insensitive to this choice (Padrino et al., 2019). By setting $\chi = 1$, boundary conditions (2.15) and (2.16) become the same as expressions (4.6) in Lockerby and Collyer (2016). Note that (2.15) results in the non-penetration condition when projected in the normal direction. If the solid's thermal conductivity is very high in comparison with the gas, e.g. as in the case of a metal, temperature deviations inside the solid can be neglected in comparison to that in the gas — i.e. $\theta_w = 0$. Otherwise, equations for the heat transfer in the solid would need to be added to the model (e.g., Young, 2011). In this work, we restrict ourselves to the case of a highly thermally conductive solid.

By introducing the total stress tensor — related to the pressure tensor of Struchtrup (2005b) —, i.e.

$$\boldsymbol{\sigma} = -p\mathbf{1} - \boldsymbol{S}, \tag{2.17}$$

which is divergence free by virtue of expression (2.2), and denoting the surface traction as $\boldsymbol{f} = \boldsymbol{n} \cdot \boldsymbol{\sigma}$, we can write (2.15) and (2.16) in a form that is more convenient for our purposes. That is,

$$\boldsymbol{u} = \boldsymbol{u}_w + C_m \frac{2-\chi}{\chi}\sqrt{\frac{\pi}{2}}\boldsymbol{f}\cdot(\mathbf{1}-\boldsymbol{nn}) - \frac{4}{15}K_{tc}\,\boldsymbol{q}\cdot(\mathbf{1}-\boldsymbol{nn}), \tag{2.18}$$

$$\theta = \theta_w + \frac{1}{4}\boldsymbol{f}\cdot\boldsymbol{n} + \frac{1}{4}p - \frac{4}{15}C_e\frac{2-\chi}{\chi}\sqrt{\frac{\pi}{2}}\,\boldsymbol{q}\cdot\boldsymbol{n}. \tag{2.19}$$

In this work, and following Lockerby and Collyer (2016), we take $\chi = 1$, corresponding to a diffusive surface, a typical value that is satisfactory for most surfaces of interest. For the remaining coefficients, we adopt the classical values ($K_{tc} = 3/4$, $C_m = 1$, and $C_e = 15/8$).

In the next section, we cast differential Equations (2.9), (2.10), and (2.14), where $\boldsymbol{w}$ and pressure p are related to the total stress tensor $\boldsymbol{\sigma}$ by means of (2.8) and (2.17), as a set of boundary integral equations.

3 Boundary integral equations for G13: Streaming flow past a solid

We consider deviations from the ground state described in the previous section caused by a streaming flow which, far from the object, has non-dimensional velocity $\boldsymbol{u}_\infty$ with respect to the laboratory frame, constant in magnitude and direction, and also by a translational motion of the object with constant velocity $\boldsymbol{u}_w$ with respect to the same frame, parallel to the free stream. Note that because of the velocity scale used to non-dimensionalize the free stream velocity, the magnitude of $\boldsymbol{u}_\infty$ is of the order of the Mach number of the free stream, which is assumed to be much smaller than one in this work. The same condition applies to the speed of the solid.

Under these considerations, we recast the system of partial differential equations of the G13 model for the deviations introduced in the previous section as a system of integral equations for a flow field bounded internally by a closed surface but otherwise unbounded with its integrals taken

over the boundary. We achieve this by exploiting the fact, evident from the previous section, that the linearized steady G13 equations can be expressed as the sum of two parts, namely, a set of Stokes-flow like equations coupled with the Laplace equation for the heat flux potential. Treating each part separately, corresponding boundary integral equations can be readily written. The coupling between the resulting integral equations is attained through the boundary conditions. It is also assumed that the pressure p, temperature θ, deviatoric stress $\boldsymbol{S}$, and heat flux $\boldsymbol{q}$ deviations vanish in the far field. Because of well-posedness considerations, an integral condition will have to be imposed restricting the application of the system of boundary integral equations to flows with certain class of fore-aft symmetry.

3.1 Stokes-flow-like equations

We note that Equations (2.9) and (2.10) have the form of the governing equations for a Stokes flow with velocity $\boldsymbol{w}$, deviatoric stress $\boldsymbol{S}$ given in (2.8) and total stress $\boldsymbol{\sigma}$ given in (2.17). Applying the Lorentz reciprocal identity (Lorentz, 1907) to this flow and to the flow given by the fundamental solution for the entire space of (2.9)-(2.10) with the former having a delta function forcing term results in the following boundary integral equation (see, e.g., Chapter 2 of Pozrikidis, 1992):

$$\frac{1}{2}\boldsymbol{w}(\boldsymbol{x}_0) = \boldsymbol{u}_\infty - \frac{1}{8\pi Kn}\int_D \boldsymbol{f}(\boldsymbol{x})\cdot\boldsymbol{G}(\boldsymbol{x},\boldsymbol{x}_0)\,dS(\boldsymbol{x}) + \frac{1}{8\pi}\fint_D \boldsymbol{w}(\boldsymbol{x})\cdot\boldsymbol{T}(\boldsymbol{x},\boldsymbol{x}_0)\cdot\boldsymbol{n}(\boldsymbol{x})\,dS(\boldsymbol{x}), \tag{3.1}$$

provided $\boldsymbol{q}$ vanishes in the far field so that $\boldsymbol{w}$ tends to $\boldsymbol{u} = \boldsymbol{u}_\infty$ there; unit vector $\boldsymbol{n}(\boldsymbol{x})$ is normal to the boundary pointing *into* the fluid. Adopting the names commonly used in the literature on boundary integral methods, point $\boldsymbol{x}$ is called an observation or field point, and $\boldsymbol{x}_0$ a pole or source point (e.g., Pozrikidis, 1992); the gas-solid surface is denoted by D. In this expression

$$\boldsymbol{G}(\boldsymbol{x},\boldsymbol{x}_0) = \frac{\mathbf{1}}{r} + \frac{(\boldsymbol{x}-\boldsymbol{x}_0)(\boldsymbol{x}-\boldsymbol{x}_0)}{r^3}, \tag{3.2}$$

is the fundamental solution or free space Green's function, also known as the Stokeslet, and

$$\boldsymbol{T}(\boldsymbol{x},\boldsymbol{x}_0) = -6\frac{(\boldsymbol{x}-\boldsymbol{x}_0)(\boldsymbol{x}-\boldsymbol{x}_0)(\boldsymbol{x}-\boldsymbol{x}_0)}{r^5}, \tag{3.3}$$

is the corresponding fundamental solution for the stress, also called the stresslet.

In expression (3.1), the crossbar on the the first integral on the right-hand side indicates that this integral exists in the principal value sense (Pozrikidis, 1992).

Unlike the case of pressure-driven flow in conduits (e.g., Rêgo-Silva et al., 1993), for external flow past either solid or fluid objects, such as drops or bubbles, to obtain a solution, an equation like (3.1) involving the surface traction suffices and a boundary integral equation for the pressure is not usually needed. For the G13 equations, because the boundary conditions involve not only the traction but also the gas pressure (see expression 2.19), an integral equation for the pressure becomes useful. A pressure equation may be written from the theory of integral equations for Stokes flow (Ladyzhenskaya, 1969; Kim and Karrila, 2005; Leal, 2007); it is presented here in a form that is free of hypersingular integrals (Ingber and Li, 1991)

$$\frac{1}{2}p(\boldsymbol{x}_0) = -\frac{1}{8\pi}\fint_D \boldsymbol{\mathcal{P}}(\boldsymbol{x}_0,\boldsymbol{x})\cdot\boldsymbol{f}(\boldsymbol{x})dS(\boldsymbol{x}) - \frac{Kn}{4\pi}\fint_D \boldsymbol{n}(\boldsymbol{x})\cdot\nabla_0\boldsymbol{\mathcal{P}}(\boldsymbol{x}_0,\boldsymbol{x})\cdot[\boldsymbol{w}(\boldsymbol{x})-\boldsymbol{w}(\boldsymbol{x}_0)]\,dS(\boldsymbol{x}) \tag{3.4}$$

where the fundamental solution for the pressure is

$$\boldsymbol{\mathcal{P}}(\boldsymbol{x}_0,\boldsymbol{x}) = -\frac{2}{r^3}(\boldsymbol{x}-\boldsymbol{x}_0), \tag{3.5}$$

and $r = |\boldsymbol{x}-\boldsymbol{x}_0|$. This vector field satisfies the vector Laplace equation when $\boldsymbol{x} \neq \boldsymbol{x}_0$, which is not

surprising as the pressure p is harmonic. Expression (3.4) can be readily obtained by considering a small nearly hemispherical volume of exclusion centered on $\boldsymbol{x}_0$ and then invoking the pressure integral equation valid when $\boldsymbol{x}_0$ is neither in the fluid volume nor on its boundary — found, for instance, in section 14.4 of Kim and Karrila (2005) — and then carrying out the standard limiting process as the hemisphere's radius tends to zero. The integral with the factor $\boldsymbol{w}(\boldsymbol{x}_0)$ is added before taking the limit using the fact that $\nabla\cdot\nabla_0\boldsymbol{\mathcal{P}}(\boldsymbol{x}_0,\boldsymbol{x}) = 0$ if $\boldsymbol{x} \neq \boldsymbol{x}_0$ (see also Ingber and Li, 1991).

There is, however, an issue with the well-posedness of expression (3.1) that needs to be addressed. The first integral on the right-hand side is a contribution to the flow represented by a single-layer potential with density $\boldsymbol{f}$. The kernel in this integral, $\boldsymbol{G}(\boldsymbol{x},\boldsymbol{x}_0)$, is such that when a vector proportional to the unit normal vector $\boldsymbol{n}(\boldsymbol{x})$ is added to a particular solution $\boldsymbol{f}(\boldsymbol{x})$, say, the resulting vector is also a solution; hence, an infinity of solutions exists for this boundary integral equation. This is equivalent to having a constant but non-zero pressure deviation in the far field. This feature of the single-layer potential is discussed in section 4.2 of Pozrikidis's (1992) textbook (see also Appendix A of Ramachandran et al., 2012). Note that because the various solutions differ by a term multiple of the normal vector, and this term produces no net force on a closed surface, the resulting drag on the body caused by the streaming flow will be unique. To obtain a unique solution for the traction $\boldsymbol{f}$, Pozrikidis (1992) advises that, if applicable, we may impose some form of spatial symmetry condition on $\boldsymbol{f}$ according to the nature of the flow and the bounding geometry. In this work we follow this path and restrict the flows to have a certain class of fore-aft symmetry and introduce an integral constraint that selects a solution such that the pressure deviation vanishes in the far field.

Suppose the solid shape and the flow around it, which satisfies the linearized steady G13 equations and associated boundary conditions, have fore-aft symmetry with respect to a plane, $z = 0$, say, and the pressure and temperature deviations vanish far from the object. In particular, assume that the normal component of the traction at the surface and the pressure field are odd functions with respect to this plane. For this flow, we have that the integral

$$\int_D \boldsymbol{f}\cdot\boldsymbol{n}\, dS = 0 \tag{3.6}$$

at the surface of the body. If we add a vector multiple of the unit normal vector, $-p_\infty\boldsymbol{n}$ say, to the surface traction, where p_∞ is a nonzero constant, this surface integral will result in $-p_\infty A_D$, where A_D is the surface of the body. Consequently, by including (3.6) in the set of boundary integral equations for the steady linearized G13 theory as a condition to be satisfied, the solution of this set will necessarily be that with vanishing pressure deviation in the far field, provided the flow satisfies the fore-aft symmetry described above. For condition (3.6) to be useful, one must know *a priori* whether the flow has the desired fore-aft symmetry. Moreover, many flows of interest will not posses such a symmetry and (3.6) will not be applicable. We will continue discussing this topic in the following section in the context of a more specific type of flow. Note however that if we are only interested in the drag on the solid, which is often the case, condition (3.6) can be dropped from the analysis.

Although in this work we focus entirely on quantities on the fluid-solid boundary, for completeness, we describe the boundary integral equations that hold at a source point $\boldsymbol{x}_0$ lying away from the boundary and inside the fluid domain. For $\boldsymbol{w}(\boldsymbol{x}_0)$, Equation (3.1) is valid except that the coefficient in the left-hand side is 1 instead of 1/2 and the integrals are both regular. Similarly, for the pressure $p(\boldsymbol{x}_0)$, expression (3.4) holds but with a coefficient of 1 appearing on the left-hand side in place of 1/2; the term $-\boldsymbol{w}(\boldsymbol{x}_0)$ within the brackets of the second integral drops out, and both integrals are regular.

3.2 Equations for the heat flux and its potential

Consider Equation (2.14). Starting with Green's second identity, after carrying out a limit calculation to take into account that point $\boldsymbol{x}_0$ belongs to boundary D, we obtain a boundary integral equation involving the heat flux potential ϕ and its normal derivative at points on D (e.g., Becker, 1992; Power

and Wrobel, 1995)

$$\frac{1}{2}\,\phi(\boldsymbol{x}_0) = \frac{1}{4\pi}\int_D \phi(\boldsymbol{x})\boldsymbol{n}(\boldsymbol{x})\cdot\nabla\mathcal{G}(\boldsymbol{x},\boldsymbol{x}_0)dS(\boldsymbol{x}) - \frac{1}{4\pi}\int_D \boldsymbol{n}(\boldsymbol{x})\cdot\nabla\phi(\boldsymbol{x})\,\mathcal{G}(\boldsymbol{x},\boldsymbol{x}_0)dS(\boldsymbol{x}), \tag{3.7}$$

where

$$\mathcal{G}(\boldsymbol{x},\boldsymbol{x}_0) = \frac{1}{r}, \tag{3.8}$$

is the fundamental solution of Laplace equation in three dimensions. In writing (3.7), we have assumed that potential ϕ vanishes far from the boundary. Note that the integrals in (3.7) exist in the classical sense as the integrands have no strong singularities (Guiggiani, 1991); they are at most weakly singular.

By taking into account definition (2.13) and the temperature jump boundary condition (2.19), expression (3.7) can be regarded as an integral equation for the normal component of the heat flux, $\boldsymbol{n}(\boldsymbol{x})\cdot\nabla\phi(\boldsymbol{x})$, on the gas side of the boundary. A boundary integral equation for the heat flux components along two mutually orthogonal directions tangential to the boundary at $\boldsymbol{x}_0$ can be obtained as follows. Assuming that source point $\boldsymbol{x}_0$ is on boundary D, we consider a volume of exclusion in the form of a spherical sector centered at $\boldsymbol{x}_0$. Now the close surface, denoted as $\widetilde{D}$, consists of the surface D minus the part of it enclosed by the volume of exclusion plus the surface of this volume enclosed by D — almost like a hemispherical surface. Since $\boldsymbol{x}_0$ now neither belongs to $\widetilde{D}$ nor to the volume enclosed by it, we may write Green's second identity for the pair $\phi(\boldsymbol{x})$ and $\mathcal{G}(\boldsymbol{x},\boldsymbol{x}_0)$ and then take its gradient with respect to $\boldsymbol{x}_0$ — denoted by ∇_0. This leads to

$$\int_{\widetilde{D}} \boldsymbol{n}(\boldsymbol{x})\cdot\boldsymbol{q}(\boldsymbol{x})\nabla_0\mathcal{G}(\boldsymbol{x},\boldsymbol{x}_0)dS(\boldsymbol{x}) - \int_{\widetilde{D}} \phi(\boldsymbol{x})\boldsymbol{n}(\boldsymbol{x})\cdot\nabla\nabla_0\mathcal{G}(\boldsymbol{x},\boldsymbol{x}_0)dS(\boldsymbol{x}) = \boldsymbol{0}. \tag{3.9}$$

We then add the term

$$\phi(\boldsymbol{x}_0)\int_{\widetilde{D}} \boldsymbol{n}(\boldsymbol{x})\cdot\nabla\nabla_0\mathcal{G}(\boldsymbol{x},\boldsymbol{x}_0)dS(\boldsymbol{x}), \tag{3.10}$$

which is zero by the divergence theorem, to the left-hand side. Carrying out the standard limiting process of taking the radius of the volume of exclusion to zero yields the boundary integral equation for the heat flux

$$\frac{1}{2}\boldsymbol{q}(\boldsymbol{x}_0) = \frac{1}{4\pi}\!\!\int_D \boldsymbol{n}(\boldsymbol{x})\cdot\boldsymbol{q}(\boldsymbol{x})\nabla\mathcal{G}(\boldsymbol{x},\boldsymbol{x}_0)dS(\boldsymbol{x}) - \frac{1}{4\pi}\!\!\int_D [\phi(\boldsymbol{x})-\phi(\boldsymbol{x}_0)]\,\boldsymbol{n}(\boldsymbol{x})\cdot\nabla\nabla\mathcal{G}(\boldsymbol{x},\boldsymbol{x}_0)dS(\boldsymbol{x}), \tag{3.11}$$

with $\boldsymbol{x}_0$ in D, and all the integrals are now Cauchy principal value integrals. The contraction of this expression with the tensor $\mathbf{1}-\boldsymbol{n}(\boldsymbol{x}_0)\boldsymbol{n}(\boldsymbol{x}_0)$ gives rise to a vector equation for the tangential components of the heat flux vector. This equation is analogous to the integral equation for the tangential heat flux proposed by Nieto et al. (2012) for transfer processes in the plane.

For a point $\boldsymbol{x}_0$ not on boundary D and inside the fluid domain, the integral equation for the heat flux potential is given by (3.7) with a factor of 1 instead of 1/2 in the term on the left-hand side (Becker, 1992). By taking the gradient with respect to $\boldsymbol{x}_0$ of this equation for the heat flux potential, we obtain the integral equation for the heat flux vector when $\boldsymbol{x}_0$ is completely inside the fluid domain.

4 Boundary integral equations for G13: Streaming flow with axial and fore-aft symmetry

In this section we specialize the boundary integrals equations presented previously to the case of streaming flow past a solid of revolution about an axis that is parallel to the direction of the free stream velocity $\boldsymbol{u}_\infty$. In addition, the solid may translate with constant speed in the direction of the free stream so that the resulting flow is axisymmetric with no swirl. Pressure and temperature deviations from the ground state approach zero in the far field. Let C be the plane curve generated by the intersection of a plane containing the axis of symmetry and the boundary D of the body. Employing

a cylindrical coordinate system (r, φ, z), where r is the radial coordinate, φ is the azimuthal angle, $0 \leqslant \varphi < 2\pi$, and z is the coordinate along the axis of symmetry, we assume, with no loss of generality, that curve C lies on plane $\varphi = 0$. Taking $dS = rd\varphi dl$, where dl is the differential arc length of C, integration in the azimuthal direction can be carried out analytically for expression (3.1), with source point $\boldsymbol{x}_0$ belonging to C, resulting in (Pozrikidis, 1992)

$$\frac{1}{2}w_\alpha(\boldsymbol{x}_0) = u_\infty^{(\alpha)} - \frac{1}{8\pi Kn}\int_C M_{\alpha\beta}(\boldsymbol{x}_0, \boldsymbol{x})\, f_\beta(\boldsymbol{x}) dl(\boldsymbol{x}) + \frac{1}{8\pi}\fint_C \mathscr{Q}_{\alpha\beta\gamma}(\boldsymbol{x}_0, \boldsymbol{x}) w_\beta(\boldsymbol{x}) n_\gamma(\boldsymbol{x})\, dl(\boldsymbol{x}), \qquad (4.1)$$

where subscripts α, β, γ can be either r or z, denoting components in the radial and axial directions, respectively; for repeated Greek indexes in a term, the summation convention applies. Now, the dimensionality of the problem is further reduced from integration about a surface in space to integration over a curve in a plane. The elements of matrices $M_{\alpha\beta}$ and $\mathscr{Q}_{\alpha\beta\gamma}$ are computed from expressions (2.4.9) and (2.4.6), respectively, of section 2.4 of the popular textbook by Pozrikidis (1992) and are not repeated here. For our purposes, it is convenient to write the traction $\boldsymbol{f}$, heat flux $\boldsymbol{q}$, and velocity $\boldsymbol{u}$ in terms of their components tangential and normal to the curve C. Let $\boldsymbol{t}$ be a unit vector tangential to C so that $\boldsymbol{t} \cdot \boldsymbol{n} = 0$; then, we may write, e.g., $\boldsymbol{f} = f_t \boldsymbol{t} + f_n \boldsymbol{n}$ or $f_\alpha = t_\alpha f_t + n_\alpha f_n$, and similarly for $\boldsymbol{q}$, $\boldsymbol{u}$, and $\boldsymbol{w}$. Introducing this decomposition into (4.1) yields

$$\begin{aligned}
&\frac{1}{2}w_t(\boldsymbol{x}_0)t_\alpha(\boldsymbol{x}_0) + \frac{1}{2}w_n(\boldsymbol{x}_0)n_\alpha(\boldsymbol{x}_0) = u_\infty^{(\alpha)} - \frac{1}{8\pi Kn}\int_C M_{\alpha\beta}(\boldsymbol{x}_0, \boldsymbol{x})\, t_\beta(\boldsymbol{x}) f_t(\boldsymbol{x}) dl(\boldsymbol{x}) \\
&-\frac{1}{8\pi Kn}\int_C M_{\alpha\beta}(\boldsymbol{x}_0, \boldsymbol{x})\, n_\beta(\boldsymbol{x}) f_n(\boldsymbol{x}) dl(\boldsymbol{x}) + \frac{1}{8\pi}\fint_C Q_{\alpha\beta}(\boldsymbol{x}_0, \boldsymbol{x}) t_\beta(\boldsymbol{x}) w_t(\boldsymbol{x})\, dl(\boldsymbol{x}) \\
&+\frac{1}{8\pi}\fint_C Q_{\alpha\beta}(\boldsymbol{x}_0, \boldsymbol{x}) n_\beta(\boldsymbol{x}) w_n(\boldsymbol{x})\, dl(\boldsymbol{x}), \qquad (4.2)
\end{aligned}$$

where

$$Q_{\alpha\beta}(\boldsymbol{x}_0, \boldsymbol{x}) = \mathscr{Q}_{\alpha\beta\gamma}(\boldsymbol{x}_0, \boldsymbol{x})\, n_\gamma(\boldsymbol{x}). \qquad (4.3)$$

Proceeding in a similar way with the pressure equation in (3.4), after integration in the azimuthal direction, we obtain

$$\begin{aligned}
&\frac{1}{2}p(\boldsymbol{x}_0) = -\frac{1}{8\pi}\fint_C \mathscr{P}_\alpha(\boldsymbol{x}_0, \boldsymbol{x}) f_\alpha(\boldsymbol{x}) dl(\boldsymbol{x}) - \frac{Kn}{4\pi}\fint_C n_\alpha(\boldsymbol{x}) \mathscr{R}_{\alpha r}(\boldsymbol{x}_0, \boldsymbol{x}) w_r(\boldsymbol{x}) dl(\boldsymbol{x}) \\
&-\frac{Kn}{4\pi}\fint_C n_\alpha(\boldsymbol{x}) \mathscr{R}_{\alpha z}(\boldsymbol{x}_0, \boldsymbol{x})\, [w_z(\boldsymbol{x}) - w_z(\boldsymbol{x}_0)]\, dl(\boldsymbol{x}) + \frac{Kn}{4\pi}\fint_C n_\alpha(\boldsymbol{x}) \mathscr{U}_{\alpha r}(\boldsymbol{x}_0, \boldsymbol{x}) w_r(\boldsymbol{x}_0) dl(\boldsymbol{x}), \qquad (4.4)
\end{aligned}$$

where

$$\begin{aligned}
&\mathscr{P}_r(\boldsymbol{x}_0, \boldsymbol{x}) = r\int_0^{2\pi} \big[\mathcal{P}_x(\boldsymbol{x}_0, \boldsymbol{x}) \cos\varphi + \mathcal{P}_y(\boldsymbol{x}_0, \boldsymbol{x}) \sin\varphi\big] d\varphi, \qquad \mathscr{P}_z(\boldsymbol{x}_0, \boldsymbol{x}) = r\int_0^{2\pi} \mathcal{P}_z(\boldsymbol{x}_0, \boldsymbol{x}) d\varphi, \\
&\mathscr{R}_{rr}(\boldsymbol{x}_0, \boldsymbol{x}) = r\int_0^{2\pi} \left[\frac{\partial \mathcal{P}_x}{\partial x_0}\cos^2\varphi + \frac{\partial \mathcal{P}_y}{\partial x_0}\cos\varphi\sin\varphi + \frac{\partial \mathcal{P}_x}{\partial y_0}\cos\varphi\sin\varphi + \frac{\partial \mathcal{P}_y}{\partial y_0}\sin^2\varphi\right] d\varphi, \\
&\mathscr{R}_{rz}(\boldsymbol{x}_0, \boldsymbol{x}) = r\int_0^{2\pi}\left[\frac{\partial \mathcal{P}_z}{\partial x_0}\cos\varphi + \frac{\partial \mathcal{P}_z}{\partial y_0}\sin\varphi\right] d\varphi, \quad \mathscr{R}_{zr}(\boldsymbol{x}_0, \boldsymbol{x}) = r\int_0^{2\pi}\left[\frac{\partial \mathcal{P}_x}{\partial z_0}\cos\varphi + \frac{\partial \mathcal{P}_y}{\partial z_0}\sin\varphi\right] d\varphi, \\
&\mathscr{R}_{zz}(\boldsymbol{x}_0, \boldsymbol{x}) = r\int_0^{2\pi}\frac{\partial \mathcal{P}_z}{\partial z_0} d\varphi, \\
&\mathscr{U}_{rr}(\boldsymbol{x}_0, \boldsymbol{x}) = r\int_0^{2\pi}\left[\frac{\partial \mathcal{P}_x}{\partial x_0}\cos\varphi + \frac{\partial \mathcal{P}_x}{\partial y_0}\sin\varphi\right] d\varphi, \qquad \mathscr{U}_{zr}(\boldsymbol{x}_0, \boldsymbol{x}) = r\int_0^{2\pi}\frac{\partial \mathcal{P}_x}{\partial z_0} d\varphi. \qquad (4.5)
\end{aligned}$$

Expressions for these integrals are given in Appendix A. Here, $\mathcal{P}_k(\boldsymbol{x}_0, \boldsymbol{x})$, with $k = x$, y, or z, denotes

the Cartesian components of vector $\boldsymbol{\mathcal{P}}(\boldsymbol{x}_0, \boldsymbol{x})$ defined in (3.5). In terms of the normal and tangential components of $\boldsymbol{f}(\boldsymbol{x})$, $\boldsymbol{w}(\boldsymbol{x})$, and $\boldsymbol{w}(\boldsymbol{x}_0)$ we have

$$\frac{1}{2}p(\boldsymbol{x}_0) = -\frac{1}{8\pi}\fint_C \mathscr{P}_\alpha(\boldsymbol{x}_0, \boldsymbol{x}) t_\alpha(\boldsymbol{x}) f_t(\boldsymbol{x}) dl(\boldsymbol{x}) - \frac{1}{8\pi}\fint_C \mathscr{P}_\alpha(\boldsymbol{x}_0, \boldsymbol{x}) n_\alpha(\boldsymbol{x}) f_n(\boldsymbol{x}) dl(\boldsymbol{x})$$
$$-\frac{Kn}{4\pi}\fint_C n_\alpha(\boldsymbol{x}) \left[\mathscr{R}_{\alpha\beta}(\boldsymbol{x}_0, \boldsymbol{x}) t_\beta(\boldsymbol{x}) w_t(\boldsymbol{x}) - \mathscr{U}_{\alpha\beta}(\boldsymbol{x}_0, \boldsymbol{x}) t_\beta(\boldsymbol{x}_0) w_t(\boldsymbol{x}_0)\right] dl(\boldsymbol{x})$$
$$-\frac{Kn}{4\pi}\fint_C n_\alpha(\boldsymbol{x}) \left[\mathscr{R}_{\alpha\beta}(\boldsymbol{x}_0, \boldsymbol{x}) n_\beta(\boldsymbol{x}) w_n(\boldsymbol{x}) - \mathscr{U}_{\alpha\beta}(\boldsymbol{x}_0, \boldsymbol{x}) n_\beta(\boldsymbol{x}_0) w_n(\boldsymbol{x}_0)\right] dl(\boldsymbol{x}), \tag{4.6}$$

with $\mathscr{U}_{\alpha z}(\boldsymbol{x}_0, \boldsymbol{x}) = \mathscr{R}_{\alpha z}(\boldsymbol{x}_0, \boldsymbol{x})$.

The boundary integral equation for the heat-flux potential for the axisymmetric case becomes

$$\frac{1}{2}\phi(\boldsymbol{x}_0) = \frac{1}{4\pi}\int_C \phi(\boldsymbol{x}) H_\alpha(\boldsymbol{x}, \boldsymbol{x}_0) n_\alpha(\boldsymbol{x}) dl(\boldsymbol{x}) - \frac{1}{4\pi}\int_C q_n(\boldsymbol{x}) G(\boldsymbol{x}, \boldsymbol{x}_0) dl(\boldsymbol{x}), \tag{4.7}$$

with $q_n(\boldsymbol{x}) = n(\boldsymbol{x}) \cdot \nabla\phi(\boldsymbol{x})$ and

$$G(\boldsymbol{x}, \boldsymbol{x}_0) = r\int_0^{2\pi} \mathcal{G}(\boldsymbol{x}, \boldsymbol{x}_0) d\varphi,$$
$$H_r(\boldsymbol{x}, \boldsymbol{x}_0) = r\int_0^{2\pi}\left[\frac{\partial\mathcal{G}}{\partial x}(\boldsymbol{x}, \boldsymbol{x}_0)\cos\varphi + \frac{\partial\mathcal{G}}{\partial y}(\boldsymbol{x}, \boldsymbol{x}_0)\sin\varphi\right] d\varphi, \quad H_z(\boldsymbol{x}, \boldsymbol{x}_0) = r\int_0^{2\pi}\frac{\partial\mathcal{G}}{\partial z}(\boldsymbol{x}, \boldsymbol{x}_0) d\varphi. \tag{4.8}$$

Expressions for these integrals are also listed in Appendix A.

Finally, after projecting vector Equation (3.11) onto unit vector $\boldsymbol{t}(\boldsymbol{x}_0)$, tangent to curve C at point $\boldsymbol{x}_0$, and introducing $q_t(\boldsymbol{x}_0) = \boldsymbol{t}(\boldsymbol{x}_0) \cdot \nabla_0\phi(\boldsymbol{x}_0)$, we obtain

$$\frac{1}{2}q_t(\boldsymbol{x}_0) = \frac{1}{4\pi}\fint_C q_n(\boldsymbol{x}) J_\alpha(\boldsymbol{x}, \boldsymbol{x}_0) t_\alpha(\boldsymbol{x}_0) dl(\boldsymbol{x}) - \frac{1}{4\pi}\fint_C [\phi(\boldsymbol{x}) - \phi(\boldsymbol{x}_0)] N_{\alpha\beta}(\boldsymbol{x}, \boldsymbol{x}_0) n_\alpha(\boldsymbol{x}) t_\beta(\boldsymbol{x}_0) dl(\boldsymbol{x}), \tag{4.9}$$

where

$$J_r(\boldsymbol{x}, \boldsymbol{x}_0) = r\int_0^{2\pi}\frac{\partial\mathcal{G}}{\partial x}(\boldsymbol{x}, \boldsymbol{x}_0) d\varphi, \qquad J_z(\boldsymbol{x}, \boldsymbol{x}_0) = r\int_0^{2\pi}\frac{\partial\mathcal{G}}{\partial z}(\boldsymbol{x}, \boldsymbol{x}_0) d\varphi,$$
$$N_{rr}(\boldsymbol{x}, \boldsymbol{x}_0) = r\int_0^{2\pi}\left(\frac{\partial^2\mathcal{G}}{\partial x^2}\cos\varphi + \frac{\partial^2\mathcal{G}}{\partial y\partial x}\sin\varphi\right) d\varphi, \quad N_{rz}(\boldsymbol{x}, \boldsymbol{x}_0) = r\int_0^{2\pi}\left(\frac{\partial^2\mathcal{G}}{\partial x\partial z}\cos\varphi + \frac{\partial^2\mathcal{G}}{\partial y\partial z}\sin\varphi\right) d\varphi,$$
$$N_{zr}(\boldsymbol{x}, \boldsymbol{x}_0) = r\int_0^{2\pi}\frac{\partial^2\mathcal{G}}{\partial z\partial x} d\varphi, \quad N_{zz}(\boldsymbol{x}, \boldsymbol{x}_0) = r\int_0^{2\pi}\frac{\partial^2\mathcal{G}}{\partial z^2} d\varphi, \tag{4.10}$$

and the results of evaluating these integrals are included in Appendix A.

Following the discussion closing sub-section 3.1 on the issue of non-uniqueness resulting from the single-layer potential in Equation (4.1), in Appendix B, we show that an axisymmetric flow with no swirl past an object of revolution with fore-aft symmetry, satisfying the linearized steady G13 equations and boundary conditions with vanishing pressure and temperature deviations in the far field and with an odd surface temperature deviation in the solid, also exhibits a certain kind of fore-aft symmetry. Specifically, the pressure deviation in the entire gas domain and the normal component of the surface traction are both odd functions with respect to the plane of (fore-aft) symmetry of the object. Therefore, by imposing condition (3.6) on this flow, for the proposed system of boundary integral equations, the solution with a pressure deviation that tends to zero far from the body will be selected. Taking into account the flow axial symmetry, after integrating along the azimuth, expression

(3.6) becomes

$$\int_C \boldsymbol{f}(\boldsymbol{x})\cdot\boldsymbol{n}(\boldsymbol{x})\, r\, dl(\boldsymbol{x}) = 0. \tag{4.11}$$

It is perhaps worth clarifying that stating a non-local constraint resulting from the fore-aft symmetry of the flow to select a particular solution is by no means restricted to the flow being axisymmetric. In this regard, and although it is beyond the scope of this work, a problem that may be worth investigating is that of streaming flow past an ellipsoid of revolution with an axis of symmetry perpendicular to the direction of the flow in the far field.

5 Numerical aspects

We use the boundary element method to obtain an approximate solution of the set of boundary integral equations. Boundary curve C is approximately described by a collection of grid points. We use straight segments to connect two consecutive grid points; each segment is designated as an element. Lying on a segment or element, we place a node midway between the element's grid points (ends). Suppose the entire curve C is discretized with N elements; there are then N nodes. We use these nodes as an approximation of the source points on the actual curve. Because we use the collocation method to generate a system of linear equations, these nodes serve as collocation points. Following the boundary-element terminology, we use 'constant' elements implying that the magnitude of a flow variable anywhere in an element is given by its value at the associated node. Note that discretization is only needed on the gas-solid boundary, and no special treatment or discretization is necessary in the far field. The kernels of the various boundary integrals contain complete elliptic integrals of the first and second kind, and these are computed with an error within 2×10^{-8} using the polynomials approximations in section 17.3 of Abramowitz and Stegun (1972). The complete elliptic integral of the first kind exhibits a logarithmic singularity when the distance between the field and collocation points tends to zero. This behaviour may influence the numerical treatment of the integral over an element as discussed in the following.

Boundary conditions (2.18) and (2.19) are introduced to the boundary integral equations through definitions (2.7) and (2.13) for $\boldsymbol{w}$ and ϕ, respectively.

After discretization of the G13 system of boundary integral equations with constant, straight elements, the resulting algebraic expressions will contain integrals with kernels that may behave differently depending on whether the collocation point belongs to the element or not. When the collocation point lies outside the interval of integration or element, the integrand is regular; when the collocation point falls in this interval, the integrand may be singular. In this regard, the singular integrands in our system will exhibit two types of singularities, namely, either a weak singularity, behaving as $\log(1/|\boldsymbol{x}-\boldsymbol{x}_0|)$ as $|\boldsymbol{x}-\boldsymbol{x}_0|\to 0$, so that the integral exists in the classical sense, or a strong singularity, behaving as $1/|\boldsymbol{x}-\boldsymbol{x}_0|$ as $|\boldsymbol{x}-\boldsymbol{x}_0|\to 0$, and the integral exists in the Cauchy principal value sense. An integrand may contain the sum of these two singularities.

The discretized form of boundary integral equation (4.2) may be written as

$$\begin{aligned}\sum_j \left[Kn^{-1}\,{}_t\widetilde{M}_{ij}^{(\alpha)} - C_m\frac{2-\chi}{\chi}\left(\frac{\pi}{2}\right)^{1/2}{}_t\widetilde{Q}_{ij}^{(\alpha)} + \frac{C_m}{2}\frac{2-\chi}{\chi}\left(\frac{\pi}{2}\right)^{1/2}t_\alpha^{(i)}\delta_{ij}\right] f_t^{(j)} + Kn^{-1}\sum_j {}_n\widetilde{M}_{ij}^{(\alpha)} f_n^{(j)} \\ - \left(\frac{2}{5}-\frac{4}{15}K_{tc}\right)\sum_j\left({}_t\widetilde{Q}_{ij}^{(\alpha)} - \frac{1}{2}t_\alpha^{(i)}\delta_{ij}\right) q_t^{(j)} - \frac{2}{5}\sum_j\left({}_n\widetilde{Q}_{ij}^{(\alpha)} - \frac{1}{2}n_\alpha^{(i)}\delta_{ij}\right) q_n^{(j)} \\ = u_\infty^{(\alpha)} - \frac{1}{2}u_w^{(\alpha,i)} + \sum_j {}_t\widetilde{Q}_{ij}^{(\alpha)}u_{wt}^{(j)} + \sum_j {}_n\widetilde{Q}_{ij}^{(\alpha)}u_{wn}^{(j)},\end{aligned} \tag{5.1}$$

where

$$ {}_t\widetilde{M}_{ij}^{(\alpha)} = \frac{1}{8\pi}\int_{C_j} M_{\alpha\beta}(\boldsymbol{x}_0^{(i)},\boldsymbol{x})t_\beta(\boldsymbol{x})dl(\boldsymbol{x}), \quad {}_n\widetilde{M}_{ij}^{(\alpha)} = \frac{1}{8\pi}\int_{C_j} M_{\alpha\beta}(\boldsymbol{x}_0^{(i)},\boldsymbol{x})n_\beta(\boldsymbol{x})dl(\boldsymbol{x}), \tag{5.2} $$

$$ {}_t\widetilde{Q}_{ij}^{(\alpha)} = \frac{1}{8\pi}\int_{C_j} Q_{\alpha\beta}(\boldsymbol{x}_0^{(i)},\boldsymbol{x})t_\beta(\boldsymbol{x})dl(\boldsymbol{x}), \quad {}_n\widetilde{Q}_{ij}^{(\alpha)} = \frac{1}{8\pi}\int_{C_j} Q_{\alpha\beta}(\boldsymbol{x}_0^{(i)},\boldsymbol{x})n_\beta(\boldsymbol{x})dl(\boldsymbol{x}). \tag{5.3} $$

Here, δ_{ij} is the Kronecker delta, equal to one when $i = j$ and zero otherwise. The sums are for $1 \leqslant j \leqslant N$. Note again that repeated Greek indexes in a term imply summation over the r and z components. The i-index denotes a collocation point and its repetition in a term does not imply summation. When $i \neq j$, the collocation point lies outside the interval of integration or element; when $i = j$, the collocation point falls in this interval. In the case of (5.1), when $i = j$, the integrands in ${}_p\widetilde{M}_{ij}^{(\alpha)}$, with $p = t$ or n, contain a weak (logarithmic) singularity whilst the integrands in ${}_p\widetilde{Q}_{ij}^{(\alpha)}$ turn out to be regular.

Boundary integral equation (4.6) leads to

$$ \begin{aligned} \sum_j \left[\widetilde{\mathscr{P}}_{ij}^{(t)} + Kn\, C_m \frac{2-\chi}{\chi}\left(\frac{\pi}{2}\right)^{1/2}\left(\widetilde{\mathscr{R}}_{ij}^{(t)} - \hat{\mathscr{U}}_i^{(t)}\delta_{ij}\right)\right] f_t^{(j)} + \sum_j \widetilde{\mathscr{P}}_{ij}^{(n)} f_n^{(j)} \\ + Kn\left(\frac{2}{5} - \frac{4}{15}K_{tc}\right)\sum_j\left(\widetilde{\mathscr{R}}_{ij}^{(t)} - \hat{\mathscr{U}}_i^{(t)}\delta_{ij}\right) q_t^{(j)} + \frac{2}{5}Kn\sum_j\left(\widetilde{\mathscr{R}}_{ij}^{(n)} - \hat{\mathscr{U}}_i^{(n)}\delta_{ij}\right) q_n^{(j)} \\ + \frac{1}{2}p_i = -Kn\sum_j\left(\widetilde{\mathscr{R}}_{ij}^{(t)} - \hat{\mathscr{U}}_i^{(t)}\delta_{ij}\right) u_{wt}^{(j)} - Kn\sum_j\left(\widetilde{\mathscr{R}}_{ij}^{(n)} - \hat{\mathscr{U}}_i^{(n)}\delta_{ij}\right) u_{wn}^{(j)}. \end{aligned} \tag{5.4} $$

In this equation

$$ \widetilde{\mathscr{P}}_{ij}^{(t)} = \frac{1}{8\pi}\!\!\int_{C_j}\!\!\mathscr{P}_\alpha(\boldsymbol{x}_0^{(i)},\boldsymbol{x})t_\alpha(\boldsymbol{x})dl(\boldsymbol{x}), \qquad \widetilde{\mathscr{P}}_{ij}^{(n)} = \frac{1}{8\pi}\int_{C_j}\mathscr{P}_\alpha(\boldsymbol{x}_0^{(i)},\boldsymbol{x})n_\alpha(\boldsymbol{x})dl(\boldsymbol{x}), \tag{5.5} $$

$$ \widetilde{\mathscr{R}}_{ij}^{(t)} = \frac{1}{4\pi}\int_{C_j} n_\alpha(\boldsymbol{x})\left[\mathscr{R}_{\alpha\beta}(\boldsymbol{x}_0^{(i)},\boldsymbol{x})t_\beta(\boldsymbol{x}) - \delta_{ij}\,\mathscr{U}_{\alpha\beta}(\boldsymbol{x}_0^{(i)},\boldsymbol{x})t_\beta(\boldsymbol{x}_0^{(i)})\right]dl(\boldsymbol{x}), \tag{5.6} $$

$$ \widetilde{\mathscr{R}}_{ij}^{(n)} = \frac{1}{4\pi}\int_{C_j} n_\alpha(\boldsymbol{x})\left[\mathscr{R}_{\alpha\beta}(\boldsymbol{x}_0^{(i)},\boldsymbol{x})n_\beta(\boldsymbol{x}) - \delta_{ij}\,\mathscr{U}_{\alpha\beta}(\boldsymbol{x}_0^{(i)},\boldsymbol{x})n_\beta(\boldsymbol{x}_0^{(i)})\right]dl(\boldsymbol{x}), \tag{5.7} $$

and

$$ \hat{\mathscr{U}}_i^{(t)} = \sum_j \widetilde{\mathscr{U}}_{ij}^{(t)}, \qquad \hat{\mathscr{U}}_i^{(n)} = \sum_j \widetilde{\mathscr{U}}_{ij}^{(n)}, \tag{5.8} $$

with

$$ \widetilde{\mathscr{U}}_{ij}^{(t)} = \frac{1}{4\pi}\int_{C_j} n_\alpha(\boldsymbol{x})\mathscr{U}_{\alpha\beta}(\boldsymbol{x}_0^{(i)},\boldsymbol{x})t_\beta(\boldsymbol{x}_0^{(i)})dl(\boldsymbol{x}), \quad \widetilde{\mathscr{U}}_{ij}^{(n)} = \frac{1}{4\pi}\int_{C_j} n_\alpha(\boldsymbol{x})\mathscr{U}_{\alpha\beta}(\boldsymbol{x}_0^{(i)},\boldsymbol{x})n_\beta(\boldsymbol{x}_0^{(i)})dl(\boldsymbol{x}), \tag{5.9} $$

when $i \neq j$, and $\widetilde{\mathscr{U}}_{ij}^{(t)} = \widetilde{\mathscr{U}}_{ij}^{(n)} = 0$, when $i = j$. The integrand in $\widetilde{\mathscr{P}}_{ij}^{(t)}$ can be written as a sum of terms with strong and weak (logarithmic) singularities; the integrand in $\widetilde{\mathscr{P}}_{ij}^{(n)}$ has a weak singularity. The integrands in $\widetilde{\mathscr{R}}_{ij}^{(t)}$ and $\widetilde{\mathscr{R}}_{ij}^{(n)}$ are also weakly singular.

Boundary integral equation (4.7) becomes

$$\frac{15}{16}Kn\sum_j\left(\widetilde{H}_{ij}-\frac{1}{2}\delta_{ij}\right)f_n^{(j)}+\sum_j\left[\widetilde{G}_{ij}-Kn\,C_e\frac{2-\chi}{\chi}\left(\frac{\pi}{2}\right)^{1/2}\left(\widetilde{H}_{ij}-\frac{1}{2}\delta_{ij}\right)\right]q_n^{(j)}$$
$$-\frac{9}{16}Kn\sum_j\left(\widetilde{H}_{ij}-\frac{1}{2}\delta_{ij}\right)p_j=-\frac{15}{4}Kn\sum_j\left(\widetilde{H}_{ij}-\frac{1}{2}\delta_{ij}\right)\theta_w^{(j)},\quad(5.10)$$

where

$$\widetilde{G}_{ij}=\frac{1}{4\pi}\int_{C_j}G(\boldsymbol{x},\boldsymbol{x}_0^{(i)})dl(\boldsymbol{x}),\qquad\widetilde{H}_{ij}=\frac{1}{4\pi}\int_{C_j}H_\alpha(\boldsymbol{x},\boldsymbol{x}_0^{(i)})\boldsymbol{n}_\alpha(\boldsymbol{x})dl(\boldsymbol{x}).\quad(5.11)$$

The integrands in both $\widetilde{G}_{ij}$ and $\widetilde{H}_{ij}$ are weakly singular.

Finally, the discrete form of expression (4.9) is

$$\frac{15}{16}Kn\sum_j\left(\widetilde{N}_{ij}-\hat{N}_i\delta_{ij}\right)f_n^{(j)}-\frac{1}{2}q_t^{(i)}+\sum_j\left[\widetilde{J}_{ij}-Kn\,C_e\frac{2-\chi}{\chi}\left(\frac{\pi}{2}\right)^{1/2}\left(\widetilde{N}_{ij}-\hat{N}_i\delta_{ij}\right)\right]q_n^{(j)}$$
$$-\frac{9}{16}Kn\sum_j\left(\widetilde{N}_{ij}-\hat{N}_i\delta_{ij}\right)p_j=-\frac{15}{4}Kn\sum_j\left(\widetilde{N}_{ij}-\hat{N}_i\delta_{ij}\right)\theta_w^{(j)},\quad(5.12)$$

where

$$\widetilde{J}_{ij}=\frac{1}{4\pi}\int_{C_j}J_\alpha(\boldsymbol{x},\boldsymbol{x}_0^{(i)})\,t_\alpha(\boldsymbol{x}_0^{(i)})\,dl(\boldsymbol{x}),\qquad\widetilde{N}_{ij}=\frac{1}{4\pi}\int_{C_j}N_{\alpha\beta}(\boldsymbol{x},\boldsymbol{x}_0^{(i)})\,n_\alpha(\boldsymbol{x})\,t_\beta(\boldsymbol{x}_0^{(i)})\,dl(\boldsymbol{x}),\quad(5.13)$$

and

$$\hat{N}_i=\sum_j\widetilde{N}_{ij}.\quad(5.14)$$

Both the integrands in $\widetilde{J}_{ij}$ and $\widetilde{N}_{ij}$ contain the sum of terms with weak and strong singularities. It should be noted that when $i=j$, according to the parenthetical expressions in (5.12), the contribution of integral $\widetilde{N}_{ij}$ to this equation cancels out. Therefore, for its numerical treatment, rather than considering this integral as having singularities, one can compute it as a regular integral.

The integrals containing either a weak (logarithmic) singularity or a strong singularity, and existing in the Cauchy principal value sense, are computed using the well-known method of singularity subtraction (e.g., see Guiggiani and Casalini, 1987), which simplifies significantly for a constant element. This technique splits the original integral into a regular integral plus a singular one that can be easily evaluated analytically. The regular integrals are numerically computed using standard Gauss-Legendre quadrature — six points are employed here.

Expressions (5.1), with $\alpha=r$ and z, (5.4), (5.10), and (5.12) form a system of $5N\times5N$ linear algebraic equations for the tangential and normal components of the traction and heat flux vectors, and the pressure on the boundary of the object.

The non-uniqueness of the solution brought by the single layer potential in equation (3.1) manifests itself in a numerical solution as a significant change in the results of some of the local variables at the boundary as the number of elements changes. As discussed in the foregoing, to alleviate this we introduced constraint (3.6) or (4.11). For the purpose of numerical implementation, (4.11) yields

$$\sum_j f_n^{(j)}\int_{C_j}r\,dl(\boldsymbol{x})=0.\quad(5.15)$$

Expression (5.15) substitutes for the r-component of expression (5.1) in a specific element. This issue is discussed further for specific problems in the next section. The final $5N\times5N$ linear system is solved using a conventional direct solver.

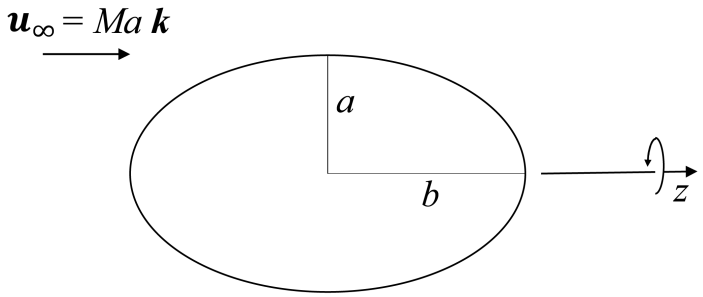

Figure 1: Streaming flow with non-dimensional speed Ma past a fixed spheroid. The spheroid is symmetric with respect to the z-axis. The sketch shows the non-dimensional semi-axes lengths a and b. For a prolate (oblate) spheroid, $a < b$ ($a > b$).

The net drag force produced on the object by the fluid stream is computed with

$$F = 2\pi \sum_j \int_{C_j} (f_t t_z + f_n n_z) r dl(\boldsymbol{x}). \tag{5.16}$$

This drag is insensitive to the non-uniqueness of the local fields and hence it retains essentially the same magnitude regardless of whether (5.15) is applied or not.

6 Application to flow past spheroids

In this section, we show results from the solution of the linearized G13 equations for steady streaming flow of rarefied gas past an ellipsoid of revolution (spheroid) fixed in space using the boundary element formulation previously described. A sketch of the flow is depicted in Fig. 1 showing a streaming flow parallel to the z-axis in the direction of increasing z; the spheroid is symmetric with respect to this axis. We denote the dimensionless magnitude of the free stream vector $\boldsymbol{u}_\infty$ as Ma. The non-dimensional lengths of the spheroid's semi-axes are denoted by a and b using the length of the smallest semi-axis as the characteristic length, which is used in computing the Knudsen number Kn. For a prolate spheroid (ovary ellipsoid), $b > a = 1$, whilst for an oblate spheroid (planetary ellipsoid), $a > b = 1$. For a streaming flow past such a geometry and satisfying the G13 equations and associated boundary conditions, assuming the temperature deviation in the solid is negligible (e.g., a highly thermally conductive material), the flow is not only axisymmetric without swirling motion but also possesses fore-aft symmetry with respect to the plane $z = 0$, perpendicular to the streaming flow and containing the spheroid's centre (see Appendix B). This symmetry is such that, by including constraint (5.15) in the numerical model, the solution corresponds, up to the error associated with the numerical approximation, to a flow with vanishing pressure deviation in the far field.

The gas-solid surface in this case is reduced to an open curve in the plane with its two ends at different locations on the z-axis. The position of the grid points corresponding to the end points of the straight elements that approximate the boundary is given in cylindrical coordinates by $r = a\sin\zeta$ and $z = b\cos\zeta$, with $\zeta = 0,\, \pi/N,\, 2\pi/N, \cdots, (N-1)\pi/N, \pi$, so that coordinate ζ is discretized with a constant step size. This discretization has the advantage of leading to a greater density of grid points or, equivalently, to shorter elements near the poles $z = \pm b$ for a prolate spheroid or near the equator $z = 0$, for an oblate spheroid. The change in the size of the elements occurs gradually for one end of the boundary to the other. We designate this discretization as the 'refined' grid. Elements of the same size result for a sphere. An alternative to the 'refined' grid is that of a 'uniform' grid, where the distance between grid points is the same for all elements. We shall make use of this grid in some instances for reasons that we shall discuss. By default, we use the 'refined' grid except where otherwise noted.

To include the global constraint (5.15) in the set of equations, we drop the r-component of

Equation (5.1) for a particular element, labeled with j_0, say, and introduce that constraint instead. Numbering the elements in ascending order from one and starting with the element having the back stagnation point as a grid point, when the total number of elements N is odd, element j_0 is given by $(N-1)/2+1$ and thus corresponds to the element bisected by plane $z=0$. On the other hand, if N is even, element j_0 is given by $N/2$, the element of the back half of the boundary that has a grid point in plane $z=0$.

In this section, when we refer to the pressure, temperature, and normal component of the traction, we are actually referring to their deviations with respect to the base (unperturbed) values. We remind the reader that the non-dimensional quantities have been defined in section 2. In this discussion, we first consider the case of flow past a sphere ($a=b=1$) as an exact solution for the G13 model is available in this case.

6.1 Sphere

For rarefied streaming flow past a sphere, the numerical solution of the G13 equations using the boundary element method can be compared with the exact theory of Young (2011) (see Appendix C of this article). This comparison is presented in Fig. 2 for Knudsen numbers $Kn=0.05$ and 0.5 showing the normal and tangential components of the traction and heat flux, temperature, pressure, and tangential component of velocity at the surface of the object. To obtain these results, we use 51 elements. Because they are proportional to Ma, with no loss of generality, we set $Ma=1$ when performing the computations. One should keep in mind that the model considered in this work is for $Ma \ll 1$. Very good match between the numerical and exact results is observed. From the physical point of view, two features that are consequence of the gas rarefaction are worth highlighting. First, Fig. 2(d) illustrates the presence of surface slip. Secondly, despite the fact that no deviation from the temperature base value is imposed either on the solid side of the boundary or in the far field and nonlinear dissipation is neglected, Figures 2(b) and (c) show non-zero heat flux profiles and a temperature jump across the gas-solid surface. The effect of temperature polarization, in which the temperature in the front and the back of the object are different, is present in the results. In our case, the temperature is odd with respect to $z=0$ and positive at the front and negative at the back. This phenomenon has been reported in the theoretical studies of Takata et al. (1993) and Torrilhon (2010) on flow past a sphere using the linearized Boltzmann equation and the regularized 13-moment theory, respectively. By taking the maximum absolute values of $u_t/(KnMa)$ and $\theta/(KnMa)$ from Figures 2(d) and (c), respectively, and multiplying them by their corresponding Kn, we note that, for the same Ma, the velocity slip and temperature jump are the highest for the largest Knudsen number, as expected. Whereas the gas velocity slip can be predicted by the NSF model with slip and jump, the temperature jump and non-zero heat flux cannot be obtained from this theory.

The accuracy of the method implemented here is investigated next by looking at the change in the average of the relative errors determined from the numerical and exact results for each element as a function of the number of elements. This is shown in Fig. 3 for the temperature, pressure, tangential and normal components of traction and heat flux, and tangential velocity on the surface of the sphere for $Kn=0.05$ and 0.5. From the interval $N=10^2$ to 10^3, we note that the change of the average relative error with the number of elements N is of the order N^{-1} for our numerical scheme making use of constant elements.

Regarding the drag on the solid sphere caused by the flowing gas, we plot in Fig. 4 the exact and numerical ($N=51$) results for this quantity, normalized by $6\pi KnMa$, for a wide range of Knudsen numbers Kn in the slip and transition regimes. The quantity $F/(6\pi KnMa)$ is equivalent to the dimensional drag F^* non-dimensionalized by the Stokes flow drag on a sphere of radius a^* with no slip, namely, $6\pi\mu_0^*|\boldsymbol{u}_\infty^*|a^*$. Very good agreement is achieved. The accuracy of the drag computation by our model is assessed in Fig. 5 where we show the relative error of the numerically determined drag with respect to the exact result as a function of the number of elements for $Kn=5\times10^{-4}$, 0.05 and 0.5. For the smallest Kn, the relative error varies according to $\sim N^{-2}$; the accuracy decreases to some extent for the intermediate value of Kn and continues deteriorating for $Kn=0.5$ to vary as $\sim N^{-1}$.

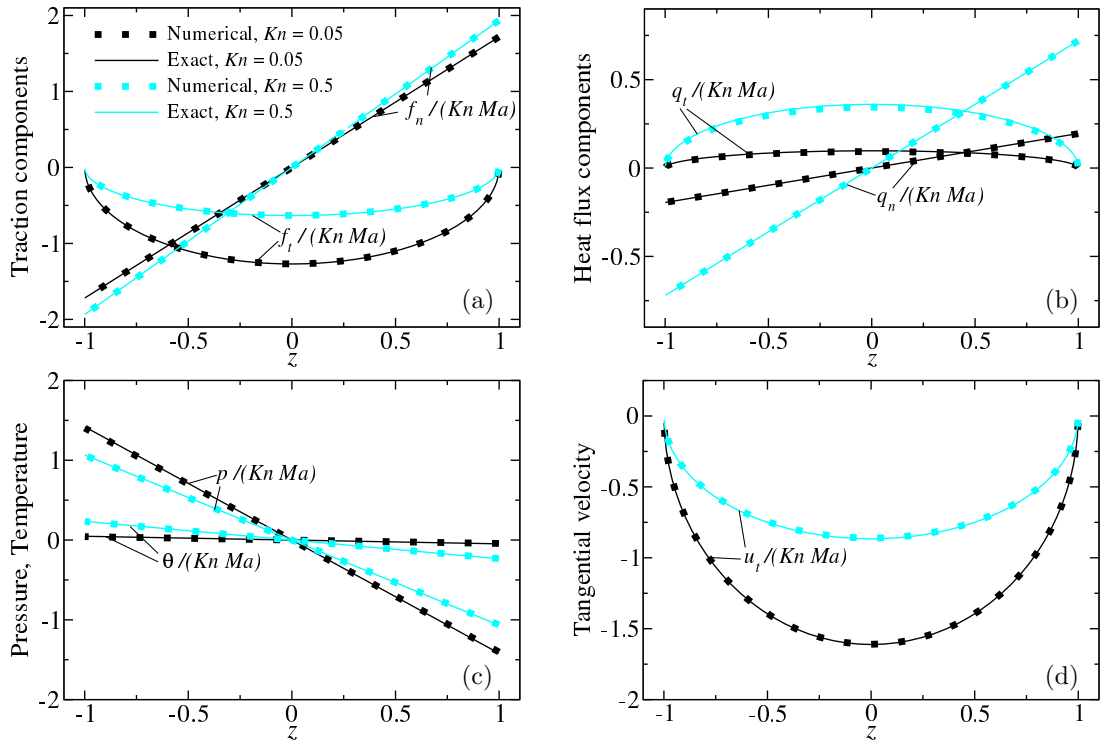

Figure 2: Numerical solution of the G13 model for the (a) tangential and normal components of the traction; (b) tangential and normal components of the heat flux; (c) pressure and temperature, and (d) tangential velocity component at the surface of a sphere in a streaming uniform flow. Numerical results are shown for $Kn = 0.05$ and 0.5 and compared with predictions from the exact theory in Young (2011). Results are normalized by the product $Kn\,Ma$, and obtained with 51 elements. The ordinate of figure (d) is equivalent to $u_t^*/(|\boldsymbol{u}_\infty^*|Kn)$, where the ' * ' refers to dimensional quantities.

Comparisons of experimental values of the drag caused on a sphere by the streaming flow of a rarefied gas with predictions from various theories are presented and discussed in the works of Torrilhon (2010), Lockerby and Collyer (2016), and Padrino et al. (2019). The last two include results from the G13 model for $Kn \leqslant 1$, which over-predicts the experiments and the results from kinetic theory in the early transition regime. Nevertheless, the theory of NSF with slip and jump results in even larger discrepancies (Lockerby and Collyer, 2016).

6.2 Spheroids: Local fields

One of the earliest and most well-known applications of the boundary element technique to low-Reynolds number flows is that by Youngren and Acrivos (1975) on streaming flow past objects with the no-slip condition considering both the axisymmetric and fully three-dimensional versions of the method. They modelled the flow with a boundary integral equation similar to expression (3.1) but with the actual fluid velocity $\boldsymbol{u}$ in place of vector $\boldsymbol{w}$. After invoking non-slip, their equation becomes an integral equation of the first kind for the surface traction. Among the examples included in their work, they considered the Stokes flow past prolate and oblate spheroids. Here, as a validation step, we present results from our numerical approach for a very small Knudsen number and compare with the analytical solution with no slip from the literature for the tangential and normal components of the traction (Brenner, 1964; Keaveny and Shelley, 2011; Padrino et al., 2020) and the pressure on the surface (Chwang and Wu, 1975; Ingber and Li, 1991). This comparison is shown in Figures 6 and 7 for a prolate (201 elements) and oblate (801 elements) spheroid, respectively, where the numerical results from G13 were obtained with $Kn = 5 \times 10^{-4}$ — Kn is computed with the length of the spheroid's smallest semi-axis. For the sake of space and clarity, we only show data for the half of the surface on the back of the body. The surface tangential traction is even with respect to $z = 0$, whilst the normal

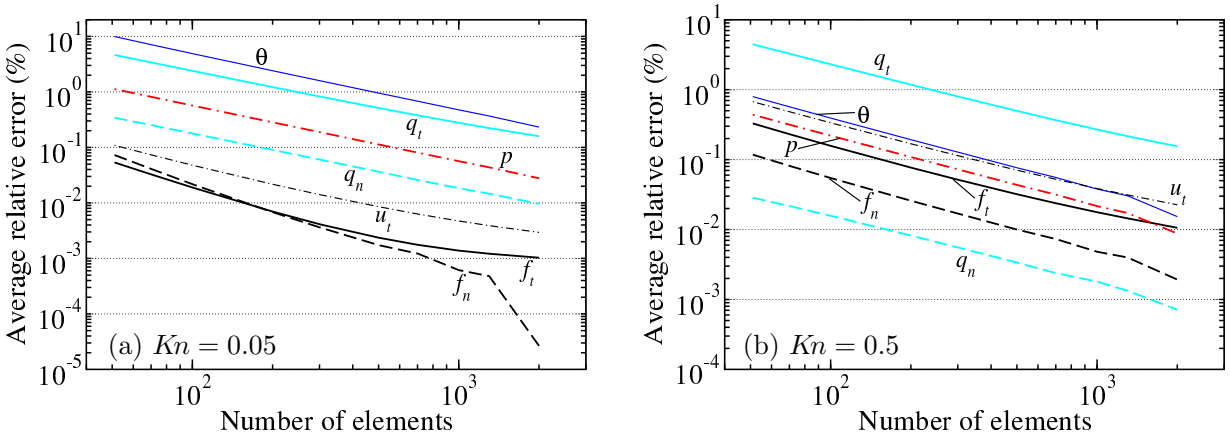

Figure 3: Average relative errors (%) of the numerical results from the G13 model for a sphere in a streaming uniform flow with respect to the exact solution as functions of the number of elements for (a) $Kn = 0.05$ and (b) $Kn = 0.5$. The figures show errors for the traction components f_t and f_n, heat flux components q_t and q_n, tangential velocity u_t, pressure p, and temperature θ on the surface of the sphere.

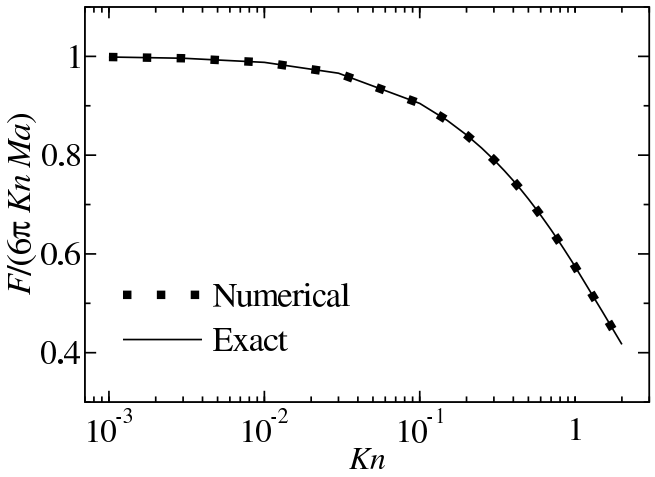

Figure 4: Drag caused by a streaming uniform flow passing a sphere as a function of the Knudsen number Kn. Numerical results were obtained with 51 elements. Results from the exact theory are included.

traction and the pressure are odd functions of z. It is observed that numerical and exact results agree very well. A shorter element size is needed in the oblate spheroid case to attain a very good match between these two solutions. A notable physical feature depicted in Fig. 6(a) is the presence of a local extremum in the profile of the tangential component of the traction occurring neither on the tail of the spheroid, $z(a/b) = 1$, nor on its equator, but at an interior point close to the tail. For the slender spheroid (case $b/a = 10$), the profile is very sharp at this extremum. A similar trend is observed in Fig. 7(b) and (c) in the case of the oblate spheroid for the pressure and normal traction — but not for the tangential traction. Such position of a local extremum does not occur in the case of flow past a sphere, as one can conclude from the analytical solution for Stokes flow with no slip that predicts a smooth variation of the tangential traction as $\sim\sqrt{1-z^2}$ and of the pressure and normal traction as $\sim z$.

The numerical results obtained by applying the boundary element method to our integral formulation of the G13 equations for rarefied flow past a prolate spheroid of aspect ratio $b/a = 3$ and 10 are presented in Fig. 8. Values of $Kn = 0.05$ and 0.5 are chosen and, since an analytical solution has not been presented for this model and flow past a spheroid, we pay special attention to the convergence of results with the number of elements; 51, 201, and 801 elements are used. Results are included for the tangential and normal components of the traction and heat flux, pressure and temperature. Again, due to the symmetry of the results, we only show them for the back half of the spheroid. Indeed,

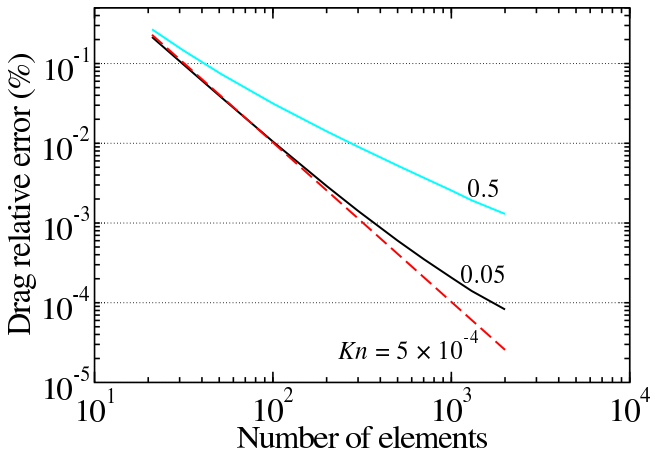

Figure 5: Relative error (%) for the drag caused by a streaming uniform flow passing a sphere computed numerically with respect to the exact result as a function of the number of elements and for three values of the Knudsen number Kn.

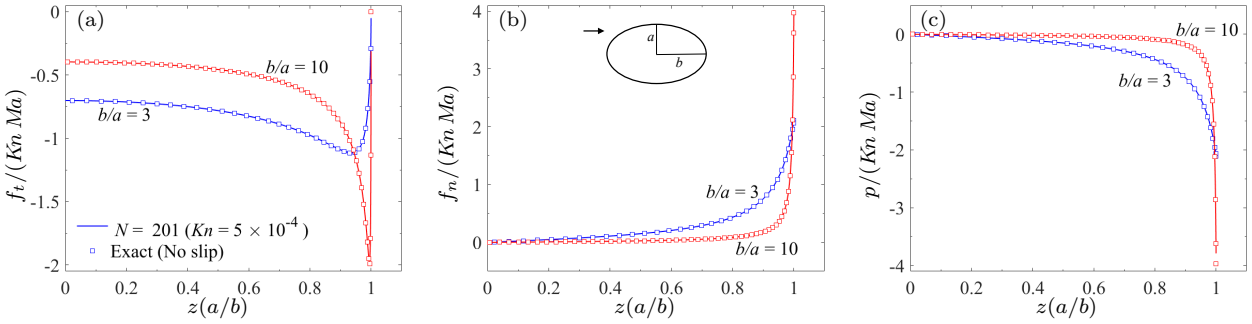

Figure 6: Numerical solution of the G13 model for $Kn = 5 \times 10^{-4}$ and a number of elements $N = 201$ for the (a) tangential and (b) normal components of the traction, and (c) pressure at the surface of a prolate spheroid with aspect ratio $b/a = 3$ and 10 in a streaming uniform flow. Results are normalized by the product $Kn\,Ma$. The exact solution for Stokes flow past a spheroid with no slip is included for comparison.

the tangential component of the surface traction and heat flux vector are even functions of z; the pressure, temperature, and normal components of the surface traction and heat flux are odd. The plots demonstrate satisfactory convergence of the results even in regions of relatively large spatial gradients for all cases considered.

The graphs of the normal components of traction and heat flux as well as the pressure and temperature in Fig. 8 show monotonic trends, for the back half of the domain, $0 \leqslant z(a/b) \leqslant 1$, although with a highly changing slope in comparison to the corresponding profiles obtained for the back of the sphere (Fig. 2). On the other hand, and unlike the sphere's case, the surface distribution of the tangential components of the traction and heat flux depicts a local extremum neither at the equatorial plane nor at the back stagnation point but very close to the latter. For the same aspect ratio, the maximum absolute values of the tangential and normal traction, tangential and normal heat flux, pressure and temperature are higher for the larger Kn. Note also that for the same Kn, the graph of every variable in Fig. 8 is much closer to zero for the largest fraction of the spatial interval $z(a/b)$ — if not for the entire span of this variable — in the case of the highest aspect ratio b/a, perhaps due to the fact that by hypothesis the temperature at the boundary on the solid side remains unperturbed in all cases.

The counterpart of Fig. 8 for the case of rarefied flow past an oblate spheroid is presented in Fig. 9 (back half of the solid object) with the same values of Knudsen number and aspect ratio, and number of elements $N = 201$, 801 and 1201. We observe a converging trend of the numerical results with increasing element number except in a small neighbourhood of $z = 0$ for the tangential

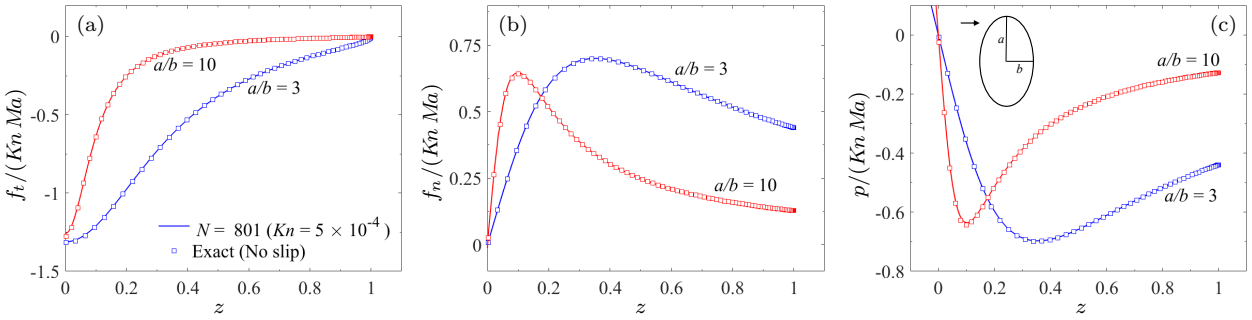

Figure 7: Numerical solution of the G13 model for $Kn = 5 \times 10^{-4}$ and a number of elements $N = 801$ for the (a) tangential and (b) normal components of the traction, and (c) pressure at the surface of an oblate spheroid with aspect ratio $a/b = 3$ and 10 in a streaming uniform flow. Results are normalized by the product $Kn\,Ma$. The exact solution for Stokes flow past a spheroid with no slip is included for comparison.

component of the heat flux and the aspect ratio $a/b = 10$. Fig. 9 also shows that, contrary to the prolate spheroid, the normal traction, normal heat-flux, pressure, and temperature exhibit a local extremum neither at the back stagnation point nor at the equator but somewhere in between, whilst the tangential traction and heat flux do show a monotonic trend in the back half of the solid geometry — the exception being the graph of $q_t/(Kn\,Ma)$ that shows a local minimum at about $z = 0.2$. As in the case of the prolate spheroid, for the same aspect ratio and for each of the physical variables, the largest of the maximum absolute values corresponds to the greater value of Kn. For the same Kn, the smallest absolute value predicted for a given variable corresponds to the largest aspect ratio for a wider z interval.

Unlike the results in Fig. 8, which were computed using a refined grid, the results in Fig. 9 were obtained utilizing a uniform grid, where the size of all the elements (straight segments) is the same. The reason for this change is that with a refined grid and utilizing $N = 801$ elements, the graphs of the normal component of the traction, pressure and temperature exhibited noticeable spurious fluctuations at and between the two physical extrema — one extremum at either side of $z = 0$ —, which became more conspicuous at the equatorial plane. The amplitude of these oscillations can be larger than the maximum of the actual absolute value of the field. We discuss the possible origin of these nonphysical oscillations below. With the uniform grid, on the other hand, significantly damped oscillations are barely noticed for the normal component of the traction, pressure and temperature for both Knudsen numbers, 1201 elements and aspect ratio $a/b = 3$, which has an element size smaller than the oblate spheroid with $a/b = 10$ and the same number of elements. For all the other cases shown in Fig. 9, oscillations are absent.

The tangential component of the velocity on the surface of the object, which characterizes the gas slip, is presented in Fig. 10 for (a) a prolate and (b) oblate spheroid, for the same conditions and number of elements used to generate Figures 8 and 9. In both cases, the graphs show convergence. The profiles of the tangential velocity are similar to those of the tangential component of the surface traction portrayed in Figures 8(a) and 9(a). This is justified after examining the relative importance of each term in the right hand side of expression (2.18). By using the numerical results, we noted for a few points that the term corresponding to the tangential component of the traction dominates over the term associated with the tangential component of the heat flux.

The extrema and the corresponding value of the coordinate where they occur for the tangential and normal components of the traction and heat flux, the pressure, and the temperature, on the surface of the back half of the particle, are presented in Fig. 11 for a prolate and in Fig. 12 for an oblate spheroid with aspect ratios 3 and 10 as function of the Knudsen number. Figure 13 shows analogous information only for the tangential component of the velocity. The focus is on the slip regime and the first part of the early transition regime. We use the superscript '+' to denote the extremum and its associated coordinate z. In the case of the prolate spheroid, the extrema for f_n, q_n, p, and θ take place

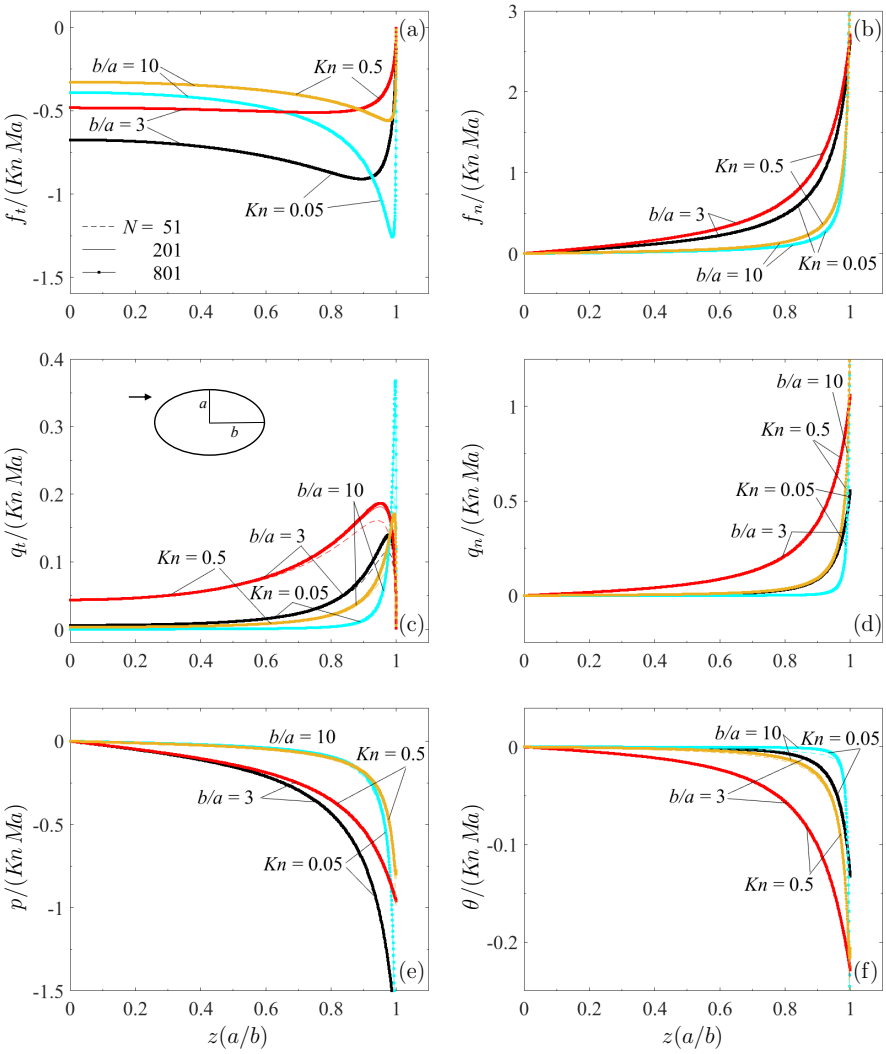

Figure 8: Numerical solution of the G13 model with three different number of elements, $N = 51$, 201, and 801, for the (a) tangential and (b) normal components of the traction; (c) tangential and (d) normal components of the heat flux; (e) pressure, and (f) temperature at the surface of a prolate spheroid with aspect ratio $b/a = 3$ and 10 in a streaming uniform flow. Results are shown for $Kn = 0.05$ and 0.5 and normalized by the product $Kn\,Ma$.

at the trailing edge of the particle, whilst for f_t, q_t, and u_t, they occur closer to the trailing edge but not at it for the lowest Kn and move towards the equator as Kn increases. For aspect ratio $b/a = 10$, the extrema are registered very near the trailing edge. For the oblate spheroid, the trends are almost the opposite of those for the prolate spheroid. Note, however, in the cases where the location of the extrema does not change with Kn, namely, the tangential component of the traction, heat flux, and velocity, $z^+ = 0$ (equator) instead of $z^+ = 1$ (trailing edge), as for the prolate particle. For both the prolate and oblate cases, for some variables and depending on the aspect ratio, the extrema may change monotonically with the Knudsen number.

To search for the possible causes of the oscillations depicted by some of the results of Fig. 9, we refer to the work of Ramachandran et al. (2012), who researched both theoretically and numerically some properties of a generalized creeping-flow, linear, boundary-integral operator consisting of single and double layer potentials arising from a vector density function. As a special case, they considered the reduced operator corresponding to Stokes flow with surface Navier slip, where the surface traction becomes the density function. By examining the eigenspectrum of this operator, Ramachandran et al. concluded that, as the mesh spacing in the numerical implementation is decreased, significant magnification of even the smallest of high-frequency errors in the forcing function should occur, leading

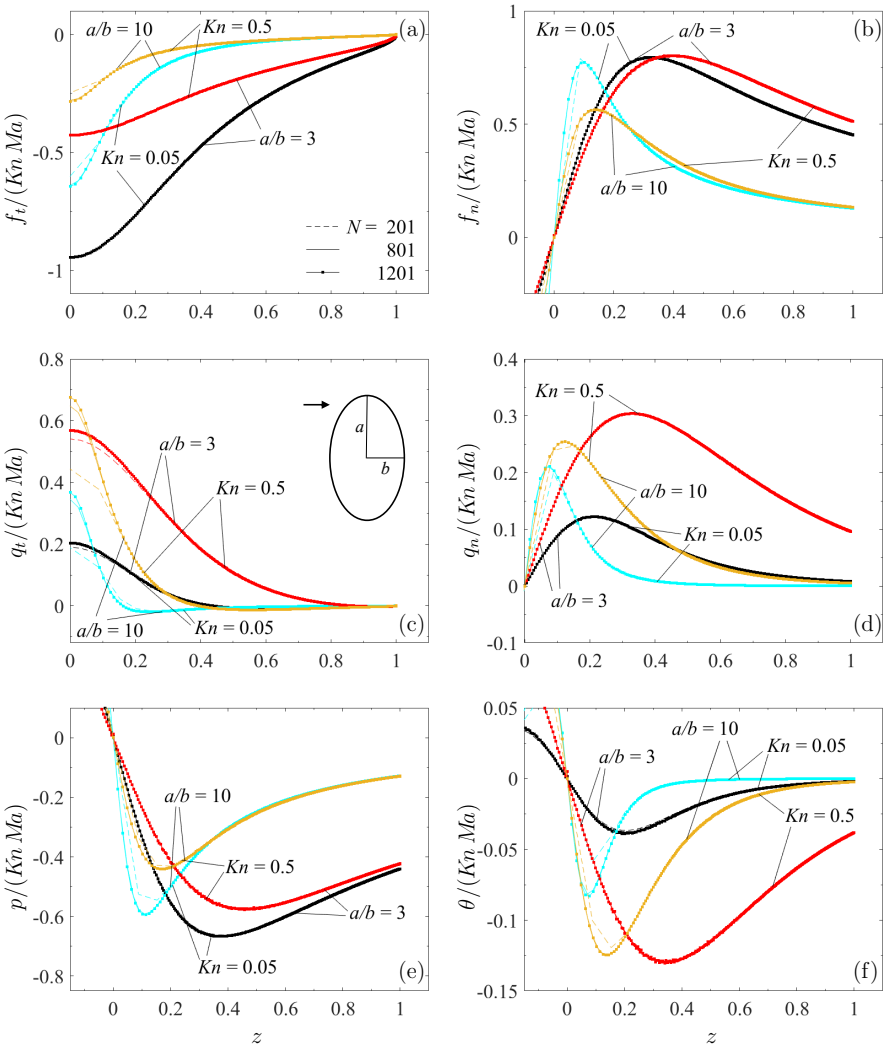

Figure 9: Numerical solution of the G13 model with three different number of elements, $N = 201$, 801, and 1201, for the (a) tangential and (b) normal components of the traction; (c) tangential and (d) normal components of the heat flux; (e) pressure, and (f) temperature at the surface of an oblate spheroid with aspect ratio $a/b = 3$ and 10 in a streaming uniform flow. Results are shown for $Kn = 0.05$ and 0.5 and normalized by the product $Kn\,Ma$.

to ill-posedness of the problem of finding the normal component of the surface traction by operator inversion (e.g., a direct method such as LU decomposition or Gauss elimination). On the other hand, they found that obtaining the tangential component of the traction can actually be a well-posed problem, although it may become ill-posed if the slip coefficient — approximately equal to Kn in our case — takes values much smaller than order one. Specifically, for the normal component of the traction, they expect the amplification factor of even relatively small errors to grow as finer meshes are used to resolve higher frequency modes, eventually leading to the corruption of the numerical solution. For a sphere, the amplification factors for the tangential and normal components of the error grow unbounded as the discretization is improved and are about the same for a zero slip coefficient (no-slip). For a sphere and both prolate and oblate spheroids, with a slip coefficient of 0.01 or higher, the amplification factor for the normal component is larger than that for the tangential component, with the difference between the two increasing with the number of elements. This difference can be of one or more orders of magnitude. While the error for the normal component of the inverted result increases without bound with mesh refinement, the error in the tangential component reaches an asymptotic value. Those authors also found out that, in comparison with a uniform mesh with the same number of elements, a refined, non-uniform mesh — such as the one used here – considerably enhances the

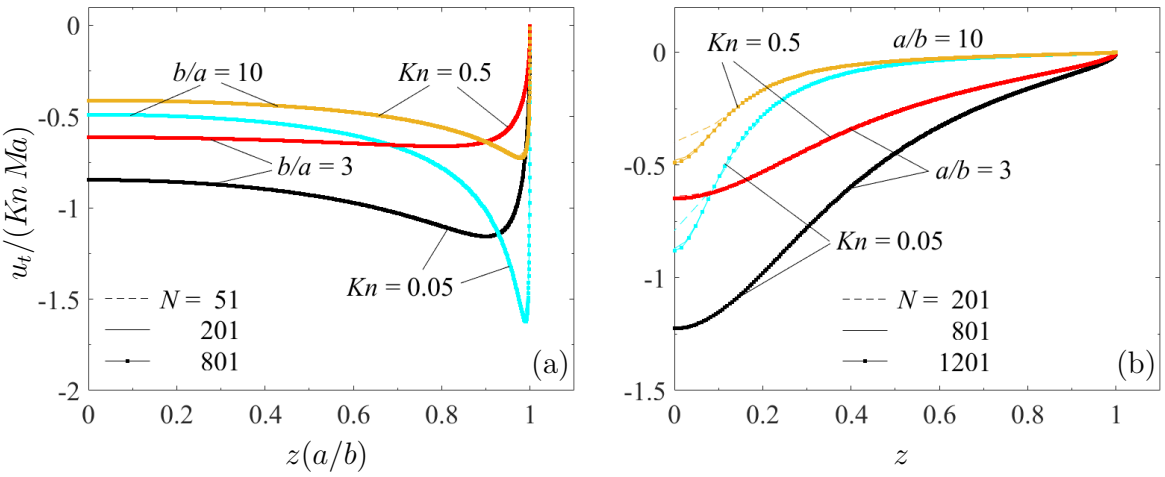

Figure 10: Numerical solution of the G13 model with three different number of elements N for the tangential component of the velocity at the surface of (a) a prolate and (b) an oblate spheroid with aspect ratios 3 and 10 in a streaming uniform flow. Results are shown for $Kn = 0.05$ and 0.5 and normalized by the product $Kn\,Ma$.

errors' amplification factors. In our results, using a refined grid, no noticeable instabilities appeared for the tangential components, neither in the traction nor in the gas velocity and heat flux, for Knudsen numbers much smaller than one, as well as about one.

Although one has to be cautious in applying the findings in Ramachandran et al. (2012) to explaining the results from the G13 theory, as those authors, obviously, did not consider the formulation proposed here, we regard as plausible that the irruption of the instabilities in the solutions may have causes similar to those pointed out by Ramachandran et al. for the slip operator and mentioned previously. To have certainty, an investigation of the eigensystem of the integral operators associated with the new boundary integral model for the G13 equations may be needed, even if only numerical on the discretized operators and not theoretical on the exact ones. This can be the subject of a full archival paper on its own. We therefore do not pursue this issue further.

As an additional test, we adapted our numerical method to the problem of axisymmetric Stokes flow past a spheroid with Navier slip. To this aim, we solve vector equation (3.1) only, with $\boldsymbol{u}$ in place for $\boldsymbol{w}$ subject to boundary condition (2.18) after dropping its last term — i.e. the heat flux contribution. Figure 14 shows the results for both a prolate and oblate spheroids of aspect ratio 5 with $Kn = 0.5$ and 51, 201, and 801 elements, using a refined grid for the prolate spheroid and a uniform grid for the oblate one. For the two largest number of elements, all curves are smooth and results show convergence.

Although not shown here, we approximated the condition of no slippage at the surface of the spheroid with both the G13 model and the model of Stokes flow with Navier slip by setting the Knudsen number $Kn = 5 \times 10^{-4}$. We considered a sphere, and prolate and oblate spheroids of aspect ratio 3 and 10. With a number of elements of 201, 801, and 1201, and utilizing a refined grid in all cases, the curves for the normal and tangential components of the traction and the pressure at the surface were smooth. Only for the oblate spheroid and 1201 elements, barely noticeable oscillations of very small amplitude were registered for the normal component of the traction. A precedent of this exercise is the application of the boundary element method by Youngren and Acrivos (1975) for streaming axisymmetric Stokes flow past spheroids (oblate and prolate) and aspect ratios up to 50 with no-slip. They reported very stable solutions (with no oscillations) for the surface traction using a number of elements up to about 40 and also 120, and collocation points equally spaced in the z direction.

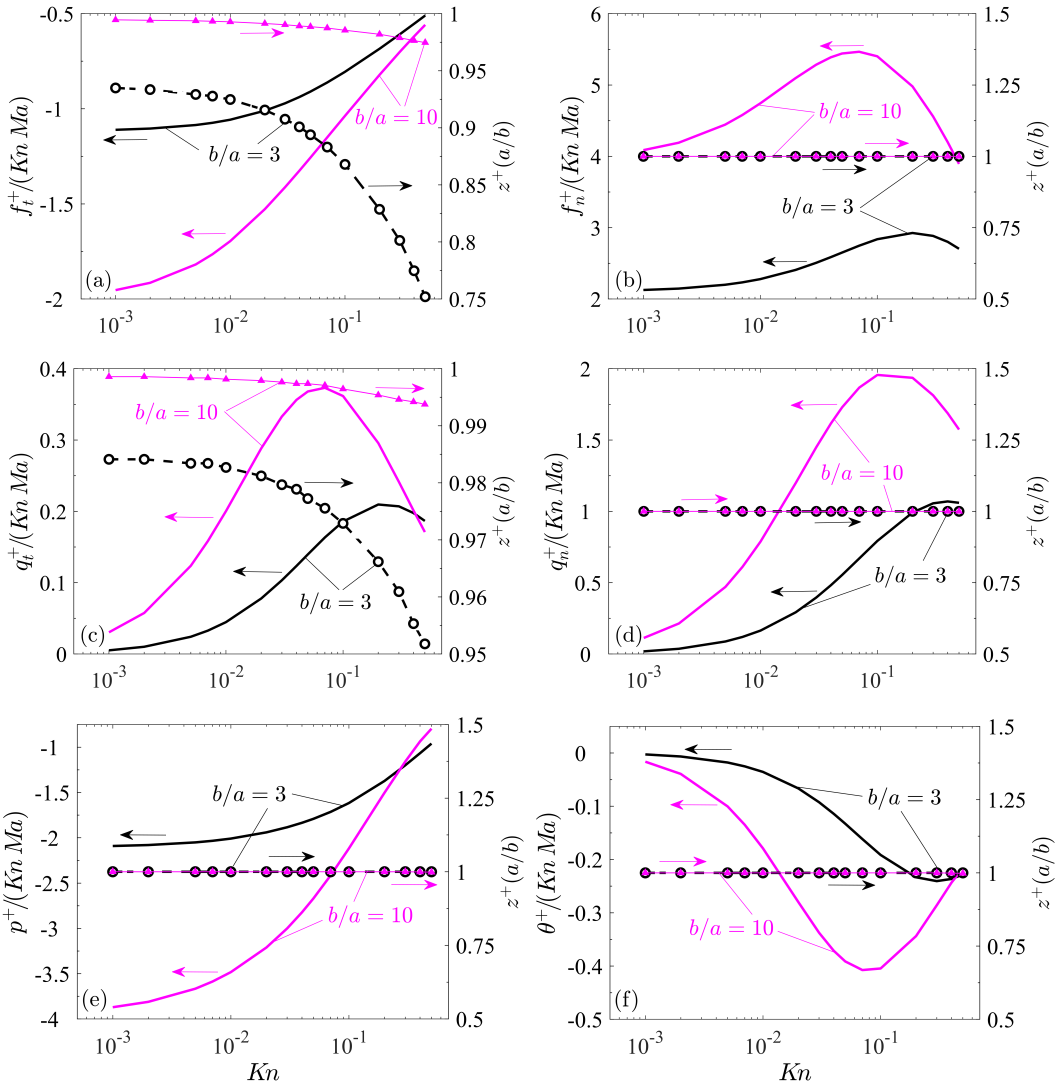

Figure 11: Extrema and their position (z^+) as function of the Knudsen number Kn from the numerical solution of the G13 model with a number of elements $N = 801$ for the (a) tangential and (b) normal components of the traction; (c) tangential and (d) normal components of the heat flux; (e) pressure, and (f) temperature at the surface of a prolate spheroid with aspect ratio $b/a = 3$ and 10 in a streaming uniform flow.

6.3 Spheroids: Drag force

The ratio of the drag produced on the spheroid by the streaming flow according to the G13 theory to the drag on a sphere with a radius equal to the spheroid's smallest semi-axis in creeping flow without slippage is plotted in Fig. 15 as a function of the Knudsen number. The numerical results from our implementation of the boundary element method are obtained with 51, 201, and 801 elements, and excellent covergence is attained, as well as very good agreement with the exact drag from classical hydrodynamics for Stokes flow with no slip when Kn tends to zero (Oberbeck, 1876; Lamb, 1932; Chwang and Wu, 1975; Happel and Brenner, 1983). The drag ratio decreases with increasing Kn for the same aspect ratio, especially in the early transition regime, and increases with the aspect ratio for the same Kn. These results are for the refined grid. They are not significantly altered when the uniform grid is used for the oblate spheroid. The largest difference with respect to the converged value is for $N = 51$ and a uniform grid for aspect ratio of 10 — i.e. the least accurate value is for the uniform grid.

It is interesting to see how results from the G13 theory compare with results from Stokes flow with Navier slip for streaming flow past a spheroid. This comparison is shown for the drag in Tables I

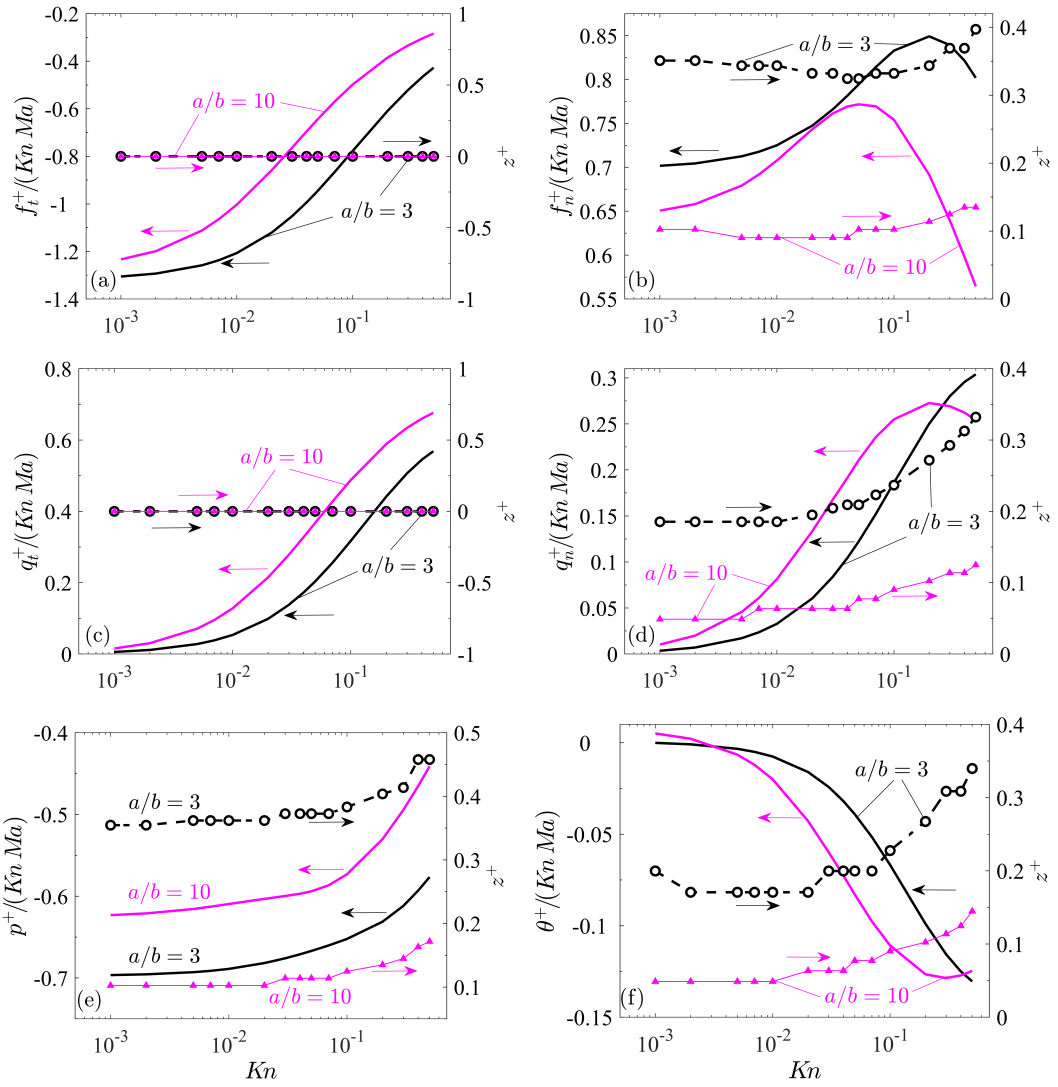

Figure 12: Extrema and their position (z^+) as function of the Knudsen number Kn from the numerical solution of the G13 model with a number of elements $N = 1201$ for the (a) tangential and (b) normal components of the traction; (c) tangential and (d) normal components of the heat flux; (e) pressure, and (f) temperature at the surface of an oblate spheroid with aspect ratio $a/b = 3$ and 10 in a streaming uniform flow.

and II for prolate and oblate spheroids, respectively, with their axes of revolution parallel to the free stream. Recall that the theory of NSF with slip and jump becomes equivalent to the model of Stokes flow with Navier slip in the case of streaming creeping flow past a solid object with no temperature differences at the boundaries. Values from the theory of Stokes flow with Navier slip are taken from the numerical results of Keh and Chang (2008). The relationship between the Knudsen number and the slip coefficient in Keh and Chang can be easily obtained, so that the comparison between the theories can be carried out. Both models are supposed to give reliable quantitative results in the slip regime but not beyond. The quantities Kn and $Kn(b/a)$ represent the Knudsen numbers computed with the length of the spheroid's semi-axis in the plane perpendicular to the streaming flow for a prolate and oblate spheroid, respectively. Based on this number, the results in the first row of Tables I and II are for flows in the slip regime (Knudsen number smaller or equal to 0.1), and they show close agreement between the theories in this condition, which seems reasonable as both theories account for slip. By contrast, the data in the second row of the tables, corresponding to flows at the end of the early transition regime (Knudsen number between 0.1 and 1), demonstrate significant differences. In all cases, lower drags are predicted by the G13 model. Interestingly, the relative difference with respect

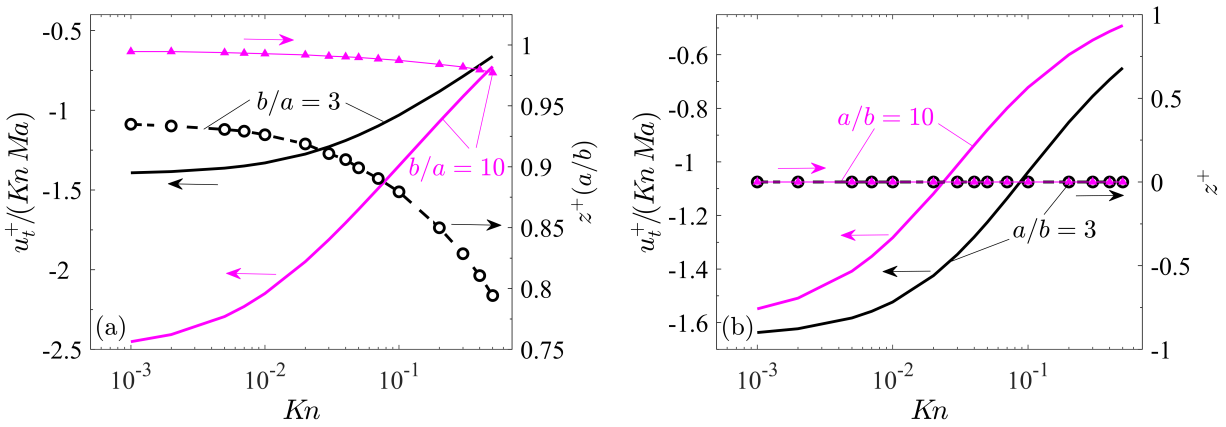

Figure 13: Extrema and their position (z^+) as function of the Knudsen number Kn from the numerical solution of the G13 model for the tangential component of the velocity at the surface of (a) a prolate ($N = 801$) and (b) an oblate spheroid ($N = 1201$) with aspect ratios 3 and 10 in a streaming uniform flow.

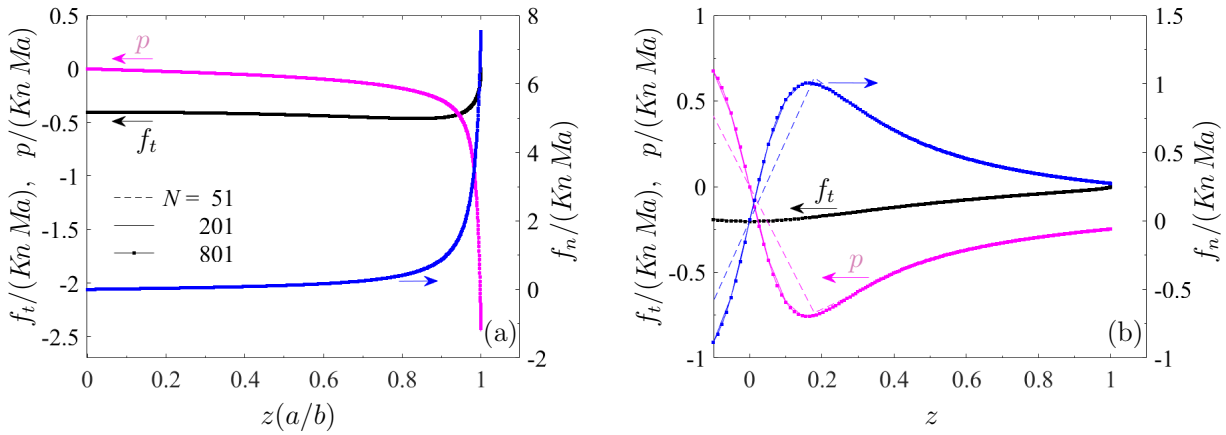

Figure 14: Numerical solution of the Stokes flow equations with Navier slip with three different number of elements, $N = 51$, 201 and 801, for the tangential and normal components of the traction and the pressure at the surface of (a) a prolate and (b) an oblate spheroid both with aspect ratio 5 in a streaming uniform flow. Results are shown for $Kn = 0.5$ and normalized by the product $Kn\,Ma$.

to the drag from the G13 model decreases as the aspect ratio b/a increases for the same Kn for the prolate geometry, whilst it increases with the aspect ratio a/b in the oblate case for the same $Kn(b/a)$. Specifically, for $Kn = 0.80$ and a prolate spheroid, the relative difference decreases from within 20% for aspect ratio $b/a = 1.1$ to within 3% for $b/a = 10$. On the other hand, for an oblate spheroid and $Kn(b/a) = 0.80$, it changes from within 23% to within 45% when the aspect ratio changes from $b/a = 0.9$ to 0.1. We may examine this trend by fixing the length of the semi-axis in the equatorial plane whilst changing the length of the semi-axis on the spheroid's axis of symmetry. Considering that the surface temperature on the solid side is uniform, increasing the ratio b/a entails increasing the surface area contacting the gas, which, in turn, would seemingly hinder the existence of temperature gradients in the gas. The opposite would be true in the oblate spheroid case when b/a is decreased. Since terms including temperature gradients or heat flux components are not part of the Stokes flow with slip model, it is when these quantities are not important that we may expect results from this theory to approximate those from the G13 model. In discussing these results, it is worth referring again to the case of streaming flow of rarefied gas past a sphere. As shown in Fig. 8 of Lockerby and Collyer (2016), the discrepancies between predictions from G13 and experimental data for the drag are notably smaller than for predictions of Stokes flow with Navier slip in the interval $0.1 \leqslant Kn \leqslant 1$. The latter predicts higher values of drag than the G13 model, the same trend observed in Tables I and

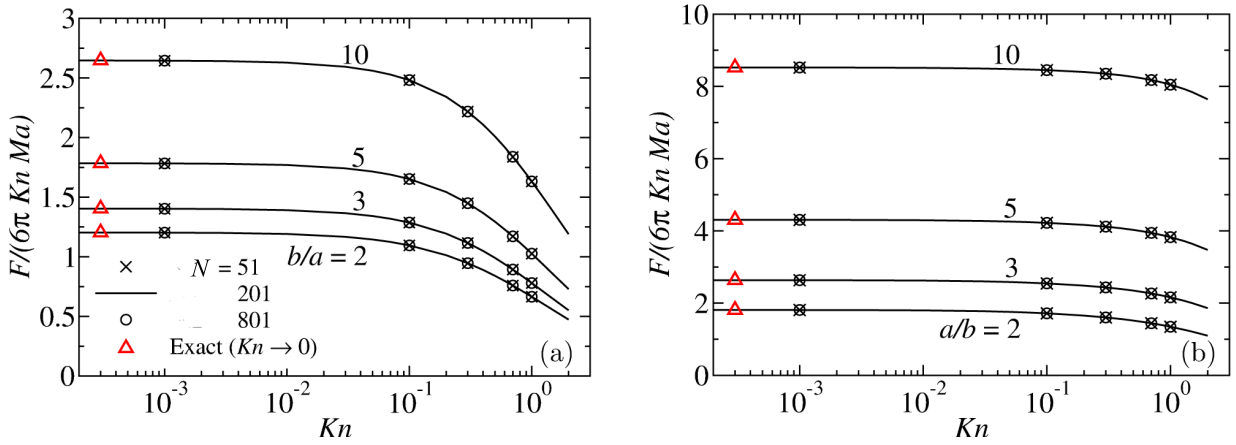

Figure 15: Drag caused by a streaming uniform flow over (a) a prolate and (b) an oblate spheroid as a function of the Knudsen number Kn from the numerical solution of the G13 model and for four aspect ratios. Results correspond to the number of elements $N = 51$, 201, and 801. Predictions from the exact theory with no slip are included. The quantity in the ordinate is equivalent to the drag on the spheroid non-dimensionalized by the drag on a sphere of radius equal to the shortest semi-axis of the spheroid in Stokes flow with no slip.

		$F/(6\pi KnMa)$			
Kn		$b/a = 1.1$	2	5	10
0.080	G13	0.9390	1.1146	1.6768	2.5129
	Stokes+slip	0.9415	1.1163	1.6783	2.5145
0.80	G13	0.6297	0.7245	1.1185	1.7641
	Stokes+slip	0.7520	0.8141	1.1750	1.8048

Table I: Drag caused on a prolate spheroid by a streaming flow parallel to its axis of revolution from the theories of G13 (present work) and Stokes flow with Navier slip (Keh and Chang, 2008).

II for a spheroid. For $Kn < 0.1$ in the sphere's case, both theories agree and predict measurements well.

As an extra validation step, we specialized our code for the case of Stokes flow with Navier slip, and applied it to the problem of axisymmetric flow past a spheroid. We simulated the conditions reported in Tables I and II here from the work of Keh and Chang (2008); our results for the drag match theirs very well.

6.4 Other features

To model Stokes flow past an object with Navier slip at the surface, the governing boundary integral equation is given by (3.1) written for the velocity instead of $\boldsymbol{w}$. With the non-penetration and slip

		$F/(6\pi KnMa(a/b))$			
$Kn(b/a)$		$b/a = 0.9$	0.5	0.2	0.1
0.080	G13	0.9021	0.8386	0.8143	0.8133
	Stokes+slip	0.9052	0.8448	0.8316	0.8396
0.80	G13	0.6142	0.5929	0.5839	0.5796
	Stokes+slip	0.7496	0.7696	0.8157	0.8355

Table II: Drag caused on an oblate spheroid by a streaming flow parallel to its axis of revolution from the theories of G13 (present work) and Stokes flow with Navier slip (Keh and Chang, 2008).

conditions, one obtains a vector equation for the tangential and normal components of the traction, whose defining linear integral operator — and also its adjoint — has the unit normal vector as a null eigenfunction. Consequently, the integral equation suffers from non-uniqueness (Ramachandran et al., 2012). A widely applied technique to remedy this is that of deflation of the operator (Pozrikidis, 1992; Kim and Karrila, 2005; Luo and Pozrikidis, 2007; Ramachandran et al., 2012). Deflation changes only the zero eigenvalue associated with the null eigenfunction without modifying the other eigenvalues and eigenvectors. As discussed in Appendix A of Ramachandran et al. (2012), this process modifies the original integral equation such that the new deflated equation now has a unique solution with the same tangential component of the traction as the original equation but with an altered normal component. Nevertheless, if one is interested in the solution with vanishing pressure in the far field, operator deflation may not necessarily return such a solution. In contrast, although only for the special case of flow with the fore-aft symmetry described here, applying a constraint such as (3.6) rather than deflation will select the solution with zero pressure at infinity.

To expose the issue of non-uniqueness introduced in the set of boundary integral equations assembled in this work by the single layer potential — integral of the traction vector — in expression (3.1), we solved the G13 equations without constraint (4.11) for the problem of streaming flow past a spheroid with its axis of revolution aligned with the free stream. We considered $Kn = 5 \times 10^{-4}$ and $Kn = 0.5$, aspect ratios of 1 and 3 (prolate and oblate, with refined and uniform grids, respectively), and number of elements of $N = 501$ and 1201. In the results for the largest Kn, we noted a significant shift by an almost constant amount of the surface profiles of the normal traction, normal heat flux, pressure, and temperature, with respect to the profiles obtained with constraint (4.11) for the sphere and oblate spheroids, with the significantly larger differences observed for $N = 1201$ than for 501. In the case of the prolate spheroid, translation of the solution occurred only for $N = 1201$ and the normal traction, pressure, and temperature profiles. This behaviour of the numerical solution is a manifestation of the ill-posedness associated with the boundary integral equation (3.1). The tangential components of the traction, velocity, and heat flux, on the other hand, remained essentially invariant with respect to including or not constraint (4.11). With $Kn = 5 \times 10^{-4}$, for the relevant variables, namely, tangential and normal traction components and pressure, we noted that the last two suffered of non-uniqueness for the sphere and oblate spheroid. On the other hand, for the prolate spheroid, these three variables showed convergence towards a unique solution. A similar exercise carried out for streaming flow over a spheroid with Navier slip and $Kn = 0.5$, showed uniqueness of the results for the tangential traction and non-uniqueness for the normal traction and pressure. As in the first case, when constraint (4.11) is not solved, the largest discrepancies with the results obtained when this expression is included were observed for the largest number of elements. By contrast, if this constraint is kept in all these examples, increasing the number of elements from 501 to 1201 caused no important differences in the results for the local variables, thereby indicating a unique solution.

As mentioned previously, the drag on the solid is insensitive to the non-uniqueness of some of the local fields manifested as large variations in their numerical results when the number of elements is drastically changed. Therefore, if we are only seeking the drag force on the solid predicted by the G13 model or by the theory of Stokes flow with Navier slip, the constraint of fore-aft symmetry in the flow can be relaxed and condition (4.11) can be dropped from the set of equations.

Regarding the computational time, for spheroids of different aspect ratios and Knudsen numbers up to 0.5, running our code in a desktop computer with an Intel® Core™ i7-6700 3.40 GHz and 8 threads with 15.6 GiB of memory, it took 29 seconds for 801 elements and less than 1 second for 201 elements.

Direct deterministic (e.g., the discrete velocity method) or stochastic (direct simulation Monte Carlo, DSMC) solutions of the Boltzmann equation require discretization of a six-dimensional phase space for steady three-dimensional flows, so they can be computationally very costly, with potentially large demands of random-access memory and relatively long running times. On the other hand, the CPU time consumed by our numerical approach for a typical case in a regular desktop, as shown here, is very short. Therefore, in the late slip or perhaps even in the early transition regimes, the

combination of theoretical formulation and numerical method presented here can be considered as a strong competitor to direct solutions of the Boltzmann equation.

7 Concluding remarks

We have considered the steady and linearized form of the G13 equations to model rarefaction effects on external gas flows past solid objects. These equations for the bulk of the flow are closed with gas-solid boundary conditions such that the resulting model is capable of predicting velocity slip, including thermal creep and thermal stress flow, and temperature jump at the boundaries. The model is applicable to situations where the Reynolds and Knudsen numbers, based on the characteristic size of the object, are much smaller and smaller than one, respectively. An example may be the flow of gas around micro- or nano-particles. Although quantitative accuracy may be limited to flows in the slip regime, qualitatively meaningful results may be expected in the early transition regime. In general, models for rarefied gases derived using the moments method (such as the G13 model) represent an improvement over the classical Navier-Stokes-Fourier model supplemented with velocity slip and temperature jump boundary conditions.

By introducing a vector and a scalar auxiliary fields, we wrote the linearized steady G13 equations governing the deviations from a ground state with the gas at rest having uniform pressure and temperature as a system that couples Stokes-flow-like equations with a Laplace equation for the scalar auxiliary variable. We then cast these partial differential equations as a set of boundary integral equations for streaming flow past a solid consisting of a vector equation coupling the gas velocity with the surface traction deviation and heat flux and a scalar equation for the pressure deviation. These equations stem from the theory of Stokes flow. They are coupled with two scalar equations obtained from the theory of harmonic potentials linking the normal and tangential components of the heat flux with a heat flux potential.

Due to the single-layer potential term in the vector integral equation linking the boundary traction deviation, velocity and heat flux derived from the theory of Stokes flow, non-uniqueness in the solution from G13 for various local fields can be expected. The non-uniqueness is associated with the fact that adding any constant to the pressure deviation in the far field still produces a solution of the system of boundary integral equations. It is manifested in the numerical solution by a change in the magnitude of local variables at the gas-solid boundary with a change in the number of elements. For flows with a certain kind of fore-aft symmetry, and following a recommendation from the literature, we exploit this attribute of the flow and showed that, by imposing a certain non-local integral constraint for the deviation in the traction normal component, the solution with vanishing far-field pressure deviation is selected. On the other hand, the drag force on the solid object is essentially insensitive to the non-uniqueness of the local surface variables as the difference in solutions for the pressure and deviatoric stress deviations causes no net force on the particle. An improved or alternative boundary integral formulation for G13 that removes the fore-aft symmetry constraint of the flow required by the present formulation would be welcome.

The boundary integral formulation for the G13 equations was reduced to the case of axisymmetric flow with no swirl of a rarefied gas past a solid and the needed forms of the fundamental solutions were derived. The boundary of interest becomes in this case a curve on the plane. To numerically solve the system of integral equations, we discretized it with the boundary element method using constant elements, leading to a set of algebraic equations that we solved with a direct technique. The formulation was then applied to the flow past a prolate or oblate spheroid held fixed and with its axis of revolution in the direction of the free stream. First, the special case of a sphere was considered for the purpose of validating the code. The comparison of the numerical results for local fields on the boundary, including temperature and pressure deviations, and the tangential component of velocity, as well as for the drag force on the particle with the exact solution of the linear G13 moment equations yielded excellent agreement. We then considered the flow past the prolate and oblate spheroids and compared the numerical solution of the G13 model in the case of a very small Knudsen number with

the exact solution from classical hydrodynamics with no slip. We introduced elements of gradually varying size that become smaller in the regions where larger gradients are expected. Overall, for the deviations in the normal and tangential components of the surface traction and the pressure, theoretical and numerical results agree very well.

For streaming gas flow past a prolate or oblate spheroid with Knudsen numbers in the slip regime and early transition regime, the numerical solution for the deviations in surface traction, heat flux, temperature, pressure, and tangential velocity showed an evident converging trend as the number of elements increased for two values of the aspect ratios, with an essentially smooth variation along the axial position. In this case, for the oblate spheroid, we discretized the boundary with elements of the same size, instead of using grid refinement, because for the latter, when the number of elements is relatively large, the graphs of the deviations for some of the variables on the surface, namely, the temperature, pressure, and normal component of the traction, exhibited noticeable spurious fluctuations that became more amplified near the equatorial plane, where the element size is the smallest. In contrast, with a uniform grid and a similar number of elements, any oscillations were significantly damped. We related the appearance of these unphysical fluctuations in the local fields to the findings in an investigation of the eigenvalues and eigenvectors of the creeping-flow boundary integral operator with slip presented in the literature. According to this work, small, high-frequency errors can be significantly amplified as the mesh discretization becomes finer, eventually rendering the inversion problem for the normal component of the traction ill-posed. On the other hand, the drag on the spheroid showed strong convergence with the number of elements for the prolate and oblate spheroids and all the aspect ratios considered for a wide interval of the Knudsen number including the early transition regime.

For rarefied gas, the numerical solution showed not only gas slip but also temperature jump with polarization at the boundary of the spheroids, a phenomenon reported in the literature from theoretical studies of gas micro-flow past a sphere. The temperature deviation was positive in the front half and negative at the back of the spheroid exhibiting odd symmetry with respect to the equatorial plane. In both halves of the spheroids — front or back —, either prolate or oblate, and unlike the sphere, some of the variables showed an interior extremum, located neither at the equatorial plane nor at the corresponding stagnation point, but at some point in between. For the prolate spheroid, the profiles of the tangential component of the traction, heat flux, and velocity have this trend. For the oblate spheroid, on the other hand, this interior extremum in a half of the solid was depicted by the deviations in the normal component of the traction and heat flux, pressure, and temperature. For a given aspect ratio, the maximum absolute value in the surface distribution of the deviation for a given variable was observed for the case with the largest Knudsen number. For a given Knudsen number, smaller absolute values of the deviation correspond to the largest aspect ratio for a wider span of the normalized axial coordinate, probably because the solid temperature was kept unperturbed.

For a fixed aspect ratio, the drag on the spheroid normalized with the Stokes-flow drag on a sphere with no slip and a radius equivalent to the spheroid's smallest semi-axis decreases with the Knudsen number in the slip and early transition regimes. For a fixed Knudsen number, the normalized drag increases with the aspect ratio for both prolate and oblate spheroids.

In the context of streaming flow of gas past a solid with no temperature gradient imposed in the far field or in the solid, for low Reynolds number flow, the Navier-Stokes-Fourier equations with velocity slip and temperature jump corrections added in the boundary conditions become equivalent to the Stokes flow equations with Navier slip. We compared results from the latter given in the literature with those from the G13 theory for the drag force. For both prolate and oblate spheroids, both sets agree for a Knudsen number, based on the length of the spheroid's semi-axis perpendicular to the flow, in the slip regime whilst some noticeable differences are obtained for a Knudsen number in the early transition regime. In addition, as a way of validation, we computed the drag on prolate and oblate spheroids caused by streaming axisymmetric Stokes flow with Navier slip by specializing our code to model this case. The newly predicted values agree with the aforementioned numerical results reported in the literature.

For a typical case, the numerical solution of the boundary integral formulation presented here is achieved very rapidly, namely, in about a few seconds. Consequently, the proposed method may be regarded as an attractive choice compared to direct deterministic or stochastic solutions (DSMC) of the Boltzmann equation.

Because the focus of this work has been on external flows at low speed with moderate rarefaction effects past objects, the proposed boundary integral equations and the numerical method of solution may find application, with minor changes, in the analysis of other external non-equilibrium phenomena, such as the process of thermophoresis on objects, caused by imposing a temperature gradient in the far field or at the boundary. On the other hand, the method can be applied, with some modifications, to the case of flow in micro- or nanochannels, where Knudsen-number effects may be relevant and the Reynolds number be negligible. These confined flows may be driven by a moving boundary, a temperature or a pressure gradient. For the latter, the seemingly new axisymmetric fundamental solutions for the pressure boundary integral equations presented here may be especially useful for flows in conduits with axial symmetry. These fundamental solutions will also be useful even in the case of low Reynolds number flows driven by a pressure gradient and modelled with the equations of classical hydrodynamics.

Acknowledgements

We acknowledge the support of the Engineering and Physical Sciences Research Council (Grant Nos. EP/N016602/1, EP/P020887/1, and EP/P031684/1) and the Leverhulme Trust (Research Project Grant).

Data availability statement

The data that support the findings of this study are openly available in [repository name] at http://doi.org/[doi], reference number [reference number].

Appendix A. Axisymmetric kernels for the pressure and heat transfer boundary integral equations

After evaluating the integrals in (4.5), the axisymmetric kernels of expression (4.4) can be written as

$$\mathscr{P}_r(\boldsymbol{x}_0,\boldsymbol{x}) = \frac{4E(m)}{\widetilde{A}^{1/2}}\left[1-\frac{2r(r-r_0)}{\widetilde{B}}\right]-\frac{4K(m)}{\widetilde{A}^{1/2}},\quad \mathscr{P}_z(\boldsymbol{x}_0,\boldsymbol{x}) = -\frac{8rE(m)(z-z_0)}{\widetilde{A}^{1/2}\widetilde{B}},$$

$$\mathscr{R}_{rr}(\boldsymbol{x}_0,\boldsymbol{x}) = \frac{8r}{\widetilde{A}^{3/2}}\left[\mathscr{I}_{30}-\frac{3}{\widetilde{A}}\{(r-r_0)^2\mathscr{I}_{50}+4r_0(r-r_0)\mathscr{I}_{52}+4r_0^2\mathscr{I}_{54}\}\right],$$

$$\mathscr{R}_{rz}(\boldsymbol{x}_0,\boldsymbol{x}) = \mathscr{R}_{zr}(\boldsymbol{x}_0,\boldsymbol{x}) = -\frac{24r(z-z_0)}{\widetilde{A}^{5/2}}\left[(r-r_0)\mathscr{I}_{50}+2r_0\mathscr{I}_{52}\right], \tag{A.1}$$

$$\mathscr{R}_{zz}(\boldsymbol{x}_0,\boldsymbol{x}) = \frac{8r}{\widetilde{A}^{3/2}}\left[\mathscr{I}_{30}-\frac{3(z-z_0)^2}{\widetilde{A}}\mathscr{I}_{50}\right],$$

and

$$\mathscr{U}_{rr}(\boldsymbol{x}_0,\boldsymbol{x}) = \frac{8r}{\widetilde{A}^{3/2}}\left[\mathscr{I}_{30}-2\mathscr{I}_{32}-\frac{3}{\widetilde{A}}\{(r-r_0)^2\left(\mathscr{I}_{50}-2\mathscr{I}_{52}\right)-4rr_0\mathscr{I}_{54}\}\right],$$

$$\mathscr{U}_{zr}(\boldsymbol{x}_0,\boldsymbol{x}) = \frac{24r(z-z_0)}{\widetilde{A}^{5/2}}\left[2r\mathscr{I}_{52}-(r-r_0)\mathscr{I}_{50}\right], \tag{A.2}$$

with

$$\mathscr{I}_{jk} = \int_0^{\pi/2} \frac{\cos^k \vartheta}{(1 - m\sin^2\vartheta)^{j/2}} d\vartheta, \tag{A.3}$$

so that

$$\mathscr{I}_{30} = \frac{E(m)}{1-m}, \quad \mathscr{I}_{32} = \frac{K(m) - E(m)}{m}, \quad \mathscr{I}_{50} = \frac{2(m_1+1)E(m)}{3m_1^2} - \frac{K(m)}{3m_1},$$
$$\mathscr{I}_{52} = \frac{(2m-1)E(m)}{3m\,m_1} + \frac{K(m)}{3m}, \quad \mathscr{I}_{54} = \frac{(m+2)}{3m^2}K(m) + \frac{2(m^2-1)}{3m^2 m_1}E(m). \tag{A.4}$$

Here,

$$\widetilde{A} = (r+r_0)^2 + (z-z_0)^2, \quad \widetilde{B} = (r-r_0)^2 + (z-z_0)^2, \quad m = \frac{4rr_0}{\widetilde{A}}, \tag{A.5}$$

and $m_1 = 1 - m = \widetilde{B}/\widetilde{A}$. Furthermore,

$$K(m) = \int_0^{\pi/2} \left(1 - m\sin^2\vartheta\right)^{-1/2} d\vartheta, \qquad E(m) = \int_0^{\pi/2} \left(1 - m\sin^2\vartheta\right)^{1/2} d\vartheta, \tag{A.6}$$

are the complete elliptic integrals of the first and second kind, respectively (Abramowitz and Stegun, 1972). In writing (A.4) we used the formulae in section 2.58 of Gradshteyn and Ryzhik (2014).

Carrying out the integrals in (4.8) results in the axisymmetric fundamental solutions corresponding to Equation (4.7), i.e.

$$G(\boldsymbol{x}, \boldsymbol{x}_0) = \frac{4r}{\widetilde{A}^{1/2}} K(m),$$
$$H_r(\boldsymbol{x}, \boldsymbol{x}_0) = \frac{2E(m)}{\widetilde{A}^{1/2}} \left[1 - \frac{2r(r-r_0)}{\widetilde{B}}\right] - \frac{2K(m)}{\widetilde{A}^{1/2}}, \qquad H_z(\boldsymbol{x}, \boldsymbol{x}_0) = -\frac{4rE(m)(z-z_0)}{\widetilde{A}^{1/2}\widetilde{B}}. \tag{A.7}$$

Finally, the integrals of (4.10) lead to the axisymmetric kernels associated with expression (4.9). These are

$$J_r(\boldsymbol{x}, \boldsymbol{x}_0) = -\frac{2rE(m)}{r_0\widetilde{A}^{1/2}} \left[1 + \frac{2r_0(r-r_0)}{\widetilde{B}}\right] + \frac{2rK(m)}{r_0\widetilde{A}^{1/2}}, \quad J_z(\boldsymbol{x}, \boldsymbol{x}_0) = -\frac{4rE(m)(z-z_0)}{\widetilde{A}^{1/2}\widetilde{B}},$$
$$N_{rr} = -\frac{4r}{\widetilde{A}^{5/2}} \left[\widetilde{A}(\mathscr{I}_{30} - 2\mathscr{I}_{32}) - 3(\mathscr{I}_{50} - 2\mathscr{I}_{52})(r-r_0)^2 + 12\mathscr{I}_{54}\, rr_0\right],$$
$$N_{rz} = \frac{12r}{\widetilde{A}^{5/2}} \left[\mathscr{I}_{50}(r-r_0) + 2\mathscr{I}_{52}r_0\right](z-z_0), \quad N_{zr} = \frac{12r}{\widetilde{A}^{5/2}} \left[\mathscr{I}_{50}(r-r_0) - 2\mathscr{I}_{52}r\right](z-z_0),$$
$$N_{zz} = -\frac{4r}{\widetilde{A}^{5/2}} \left[\widetilde{A}\mathscr{I}_{30} - 3\mathscr{I}_{50}(z-z_0)^2\right]. \tag{A.8}$$

Appendix B. Flow fore-aft symmetry

In this appendix we show that the flow described in Section 4 possesses fore-aft symmetry. Consider the flow and temperature fields resulting from a streaming rarefied gas motion with velocity $u_\infty \boldsymbol{k}$ past a rigid body with axial symmetry about the z-axis ($\boldsymbol{k}$-direction) that also translate with velocity $u_w \boldsymbol{k}$. The body exhibits fore-aft symmetry with respect to a plane, $z = 0$, say. For simplicity, suppose that our frame of reference now moves with the free stream. Also, suppose that these fields solve the G13

equations (2.1)-(2.5) with boundary conditions

$$\boldsymbol{u}\cdot\boldsymbol{n} = \widetilde{\boldsymbol{u}}_w\cdot\boldsymbol{n}, \tag{B.1}$$

$$\boldsymbol{u}\cdot\boldsymbol{t} = \widetilde{\boldsymbol{u}}_w\cdot\boldsymbol{t} + C_m\frac{2-\chi}{\chi}\sqrt{\frac{\pi}{2}}\boldsymbol{f}\cdot\boldsymbol{t} - \frac{4}{15}K_{tc}\,\boldsymbol{q}\cdot\boldsymbol{t}, \tag{B.2}$$

obtained from (2.18), with $\widetilde{\boldsymbol{u}}_w = (u_w - u_\infty)\boldsymbol{k}$, plus the temperature jump condition (2.19) with prescribed θ_w. Here, $\boldsymbol{t}$ is a unit vector tangential to the surface of the body of revolution and both $\boldsymbol{n}$ and $\boldsymbol{t}$ belong to the same plane, which also contains the z-axis. We assume that the deviations from the ground state, including the pressure and temperature deviations, vanish in the far field. The gas is therefore at rest there in the new frame of reference. Furthermore, the body temperature at its surface is prescribed to be an odd function with respect to the symmetry plane $z = 0$.

Using cylindrical coordinates, with r and z being the radial and axial coordinates, respectively, reflecting the flow field around $z = 0$ by negating the z-components of the vectors, whilst the radial components and scalars are unchanged, yields

$$\begin{aligned}
p'(r,z) &= p(r,-z), & \theta'(r,z) &= \theta(r,-z),\\
u'_r(r,z) &= u_r(r,-z), & u'_z(r,z) &= -u_z(r,-z),\\
q'_r(r,z) &= q_r(r,-z), & q'_z(r,z) &= -q_z(r,-z),\\
f'_r(r,z) &= f_r(r,-z), & f'_z(r,z) &= -f_z(r,-z),
\end{aligned} \tag{B.3}$$

where the traction components f_r and f_z and their corresponding primed counterparts exist only at the surface of the body.

By direct substitution, one can show that the primed variables in (B.3) solve the steady, linearized G13 equations and its associated boundary conditions provided the flow is reversed, that is $\widetilde{\boldsymbol{u}}_w$ is set to $(u_\infty - u_w)\boldsymbol{k}$ in (B.1) and (B.2); the surface temperature is set to $\theta_w(r,-z)$ in (2.19), and unit vectors $\boldsymbol{n}'$ and $\boldsymbol{t}'$ are substituted for $\boldsymbol{n}$ and $\boldsymbol{t}$, respectively, in these boundary conditions, with $n'_r(r,z) = n_r(r,-z)$ and $n'_z(r,z) = -n_z(r,-z)$, and similar expressions for the components of $\boldsymbol{t}'$.

Given the system is linear, the result of multiplying the original solution by -1 must also be a solution if the surface velocity is reversed to $(u_\infty - u_w)\boldsymbol{k}$ and the surface temperature of the solid becomes $-\theta_w(r,z)$. Because, by hypothesis, the body temperature at the boundary is odd, i.e. $\theta_w(r,-z) = -\theta_w(r,z)$, both solutions satisfy the same equations in the bulk and the same boundary conditions. They can thus be equated, yielding

$$\begin{aligned}
p(r,z) &= -p(r,-z), & \theta(r,z) &= -\theta(r,-z),\\
u_r(r,z) &= -u_r(r,-z), & u_z(r,z) &= u_z(r,-z),\\
q_r(r,z) &= -q_r(r,-z), & q_z(r,z) &= q_z(r,-z),\\
f_r(r,z) &= -f_r(r,-z), & f_z(r,z) &= f_z(r,-z).
\end{aligned} \tag{B.4}$$

Therefore, the scalars p and θ are odd functions of z as well as the radial components of the vectors $\boldsymbol{u}$, $\boldsymbol{q}$, and $\boldsymbol{f}$, whereas the axial components are even functions. An immediate consequence of these symmetries is that

$$\int_D \boldsymbol{f}\cdot\boldsymbol{n}\,dS = 0 \tag{B.5}$$

at the surface of the body, given that n_r is even and n_z is odd.

Appendix C. Exact solution of the linearized G13 equations: Streaming flow past a sphere

The exact solution of the linearized G13 equations for rarefied streaming flow past a sphere was given by Young (2011). In dimensionless form, consider a solid sphere of unit radius; far from the sphere,

the flow is uniform with speed Ma and in the direction of the z-axis (from left to right). The sphere is kept fixed and at an uniform temperature (highly thermally conductive sphere). In the far field, the fluid pressure and temperature are uniform and remain unperturbed by the presence of the object, and the temperature is the same as that of the sphere. The flow and temperature fields resulting from the inclusion of the sphere are modelled through Equations (2.1)-(2.5) with boundary conditions (2.15)-(2.16) at the surface of the sphere. In spherical-polar coordinates (ϱ, ϑ) with radial coordinate ϱ and angle $0 \leqslant \vartheta \leqslant \pi$ and with origin at the centre of the sphere, the radial and tangential components of velocity are

$$u_\varrho = -\frac{6A_0 + (B_0 - 3\varrho)\varrho^2}{3\varrho^3} Ma \cos\vartheta, \tag{C.1}$$

$$u_\vartheta = -\frac{6A_0 - (B_0 - 6\varrho)\varrho^2}{6\varrho^3} Ma \sin\vartheta, \tag{C.2}$$

respectively. The pressure and temperature deviations with respect to the far-field values are given by

$$p = -\frac{B_0}{3\varrho^2} KnMa \cos\vartheta, \tag{C.3}$$

$$\theta = \frac{C_0}{\varrho^2} Ma \cos\vartheta, \tag{C.4}$$

respectively. The radial and tangential components of the heat flux are

$$q_\varrho = \frac{15\, C_0 + 2B_0 Kn}{2\varrho^3} KnMa \cos\vartheta, \tag{C.5}$$

$$q_\vartheta = \frac{15\, C_0 + 2B_0 Kn}{4\varrho^3} KnMa \sin\vartheta, \tag{C.6}$$

and the components of the deviatoric stress tensor can be written as

$$S_{\varrho\varrho} = -\frac{180A_0 - 18Kn(15C_0 + 2B_0 Kn) + 10B_0\varrho^2}{15\varrho^4} KnMa \cos\vartheta, \tag{C.7}$$

$$S_{\varrho\vartheta} = -\frac{30A_0 - 3Kn(15C_0 + 2B_0 Kn)}{5\varrho^4} KnMa \sin\vartheta, \tag{C.8}$$

$$S_{\vartheta\vartheta} = \frac{90A_0 - 9Kn(15C_0 + 2B_0 Kn) + 5B_0\varrho^2}{15\varrho^4} KnMa \cos\vartheta, \tag{C.9}$$

where

$$A_0 = -\frac{40 + 126Kn^2 + 75Kn\sqrt{2\pi} - 324Kn^3\sqrt{2\pi}}{160 + 540Kn\sqrt{2\pi} + 648Kn^3\sqrt{2\pi} + 36Kn^2(18 + 25\pi)}, \tag{C.10}$$

$$B_0 = \frac{45\left[8 + 23Kn\sqrt{2\pi} + 30Kn^2(1 + \pi)\right]}{80 + 270Kn\sqrt{2\pi} + 324Kn^3\sqrt{2\pi} + 18Kn^2(18 + 25\pi)}, \tag{C.11}$$

$$C_0 = -\frac{30Kn^2\left[4\sqrt{2\pi} + 108Kn^3(1 + \pi) + 9Kn^2\sqrt{2\pi}\,(7 + 5\pi) + 3Kn(8 + 13\pi)\right]}{\left(8 + 36Kn^2 + 15Kn\sqrt{2\pi}\right)\left[40 + 135Kn\sqrt{2\pi} + 162Kn^3\sqrt{2\pi} + 9Kn^2(18 + 25\pi)\right]}. \tag{C.12}$$

Finally, the total drag acting on the sphere is

$$F = \frac{6\pi KnMa\left[40 + 115Kn\sqrt{2\pi} + 150Kn^2\,(1 + \pi)\right]}{40 + 9Kn\left[15\sqrt{2\pi} + Kn\left(18 + 25\pi + 18Kn\,\sqrt{2\pi}\right)\right]}, \tag{C.13}$$

and the ratio $F/(6\pi KnMa) \to 1$ when $Kn \to 0$. This is the same expression as in Lockerby and Collyer (2016), where they correct the corresponding expression obtained by Young (2011). Note that the Knudsen number in the papers by Young (2011) and Lockerby and Collyer (2016) is $\sqrt{\pi/2}\,Kn$.

References

Abramowitz, M. and Stegun, I. (1972). *Handbook of mathematical functions with formulas, graphs, and mathematical tables (10th printing)*. U.S. Department of Commerce, National Bureau of Standards.

Agarwal, R. K., Yun, K.-Y., and Balakrishnan, R. (2001). Beyond Navier-Stokes: Burnett equations for flows in the continuum–transition regime. *Physics of Fluids*, 13(10):3061–3085.

Bassett, A. B. (1888). *A treatise on hydrodynamics*. Cambridge University Press (Reprinted by Dover, 1961).

Becker, A. A. (1992). *The boundary element method in engineering: A complete course*, volume 19. McGraw-Hill London.

Bosworth, R. W., Ventura, A., Ketsdever, A., and Gimelshein, S. (2016). Measurement of negative thermophoretic force. *Journal of Fluid Mechanics*, 805:207–221.

Brenner, H. (1964). The Stokes resistance of an arbitrary particle – IV Arbitrary fields of flow. *Chemical Engineering Science*, 19(10):703–727.

Chang, Y. C. and Keh, H. J. (2009a). Thermophoresis of axisymmetric aerosol particles along their axes of revolution. *AIChE journal*, 55(1):35–48.

Chang, Y. C. and Keh, H. J. (2009b). Translation and rotation of slightly deformed colloidal spheres experiencing slip. *Journal of colloid and interface science*, 330(1):201–210.

Chwang, A. T. and Wu, T. (1975). Hydromechanics of low-Reynolds-number flow. Part 2. Singularity method for Stokes flows. *Journal of Fluid Mechanics*, 67(4):787–815.

Claydon, R., Shrestha, A., Rana, A. S., Sprittles, J. E., and Lockerby, D. A. (2017). Fundamental solutions to the regularised 13-moment equations: Efficient computation of three-dimensional kinetic effects. *Journal of Fluid Mechanics*, 833.

Corriveau, J. L. (2016). Aerobiological aspects of biological warfare. In Salem, H. and Katz, S. A., editors, *Aerobiology: The toxicology of airborne pathogens and toxins*, Issues in Toxicology No. 25, chapter 9, pages 330–344. Royal Society of Chemistry.

Dwyer, H. A. (1967). Thirteen-moment theory of the thermal force on a spherical particle. *The Physics of Fluids*, 10(5):976–984.

Frangi, A. (2012). Fast Stokes solvers for MEMS. In Langer, U., Schanz, M., Steinbach, O., and Wendland, W., editors, *Fast Boundary Element Methods in Engineering and Industrial Applications*, pages 221–240. Springer.

Frangi, A., Spinola, G., and Vigna, B. (2006). On the evaluation of damping in MEMS in the slip–flow regime. *International Journal for Numerical Methods in Engineering*, 68(10):1031–1051.

Grad, H. (1949). On the kinetic theory of rarefied gases. *Communications on pure and applied mathematics*, 2(4):331–407.

Gradshteyn, I. S. and Ryzhik, I. M. (2014). *Table of integrals, series, and products*. Academic Press. (Zwillinger, D. and Moll, V., editors).

Gu, X. and Emerson, D. (2007). A computational strategy for the regularized 13 moment equations with enhanced wall-boundary conditions. *Journal of Computational Physics*, 225(1):263–283.

Guiggiani, M. (1991). The evaluation of Cauchy principal value integrals in the boundary element method—A review. *Mathematical and Computer Modelling*, 15(3-5):175–184.

Guiggiani, M. and Casalini, P. (1987). Direct computation of Cauchy principal value integrals in advanced boundary elements. *International Journal for Numerical Methods in Engineering*, 24(9):1711–1720.

Happel, J. and Brenner, H. (1983). *Low Reynolds number hydrodynamics – With special applications to particulate media*. Martinus Nijhoff Publishers, The Hague, The Netherlands.

Heiken, G. (1994). Volcanic ash: What it is and how it forms. In *Volcanic Ash and Aviation SafetyProceedings of the First International Symposium on Volcanic Ash and Aviation Safety*, U.S. Geological Survey Bulletin 2047, pages 39–45.

Ingber, M. S. and Li, J. (1991). Surface pressure solution for boundary-element analysis of Stokes flow. *Communications in Applied Numerical Methods*, 7(5):367–376.

Kandlikar, S., Garimella, S., Li, D., Colin, S., and King, M. R. (2014). *Heat transfer and fluid flow in minichannels and microchannels*. Elsevier.

Karniadakis, G., Beskok, A., and Aluru, N. (2005). *Microflows and nanoflows: Fundamentals and simulation*, volume 29. Springer Science & Business Media.

Keaveny, E. E. and Shelley, M. J. (2011). Applying a second-kind boundary integral equation for surface tractions in Stokes flow. *Journal of Computational Physics*, 230(5):2141–2159.

Keh, H. J. and Chang, Y. C. (2008). Slow motion of a slip spheroid along its axis of revolution. *International Journal of Multiphase Flow*, 34(8):713–722.

Keh, H. J. and Huang, C. H. (2004). Slow motion of axisymmetric slip particles along their axes of revolution. *International Journal of Engineering Science*, 42(15-16):1621–1644.

Keh, H. J. and Ou, C. L. (2004). Thermophoresis of aerosol spheroids. *Aerosol Science and Technology*, 38(7):675–684.

Kesavan, J., Montoya, L. D., and Laube, B. L. (2016). Aerosol physics for bioaerosols. In Salem, H. and Katz, S. A., editors, *Aerobiology: The toxicology of airborne pathogens and toxins*, Issues in Toxicology No. 25, chapter 10, pages 345–370. Royal Society of Chemistry.

Kim, S. and Karrila, S. J. (2005). *Microhydrodynamics: Principles and selected applications*. Dover Publications.

Ladyzhenskaya, O. A. (1969). *The mathematical theory of viscous incompressible flow*. Gordon and Breach.

Lamb, H. (1932). *Hydrodynamics*. Dover Publications, New York, 6th edition.

Leal, L. G. (2007). *Advanced transport phenomena: Fluid mechanics and convective transport processes*. Cambridge University Press.

Leong, K. H. (1984). Thermophoresis and diffusiophoresis of large aerosol particles of different shapes. *Journal of Aerosol Science*, 15(4):511–517.

Lighty, J. S., Veranth, J. M., and Sarofim, A. F. (2000). Combustion aerosols: Factors governing their size and composition and implications to human health. *Journal of the Air & Waste Management Association*, 50(9):1565–1618.

Lockerby, D. A. and Collyer, B. (2016). Fundamental solutions to moment equations for the simulation of microscale gas flows. *Journal Fluid Mechanics*, 806:413–436.

Lorentz, H. A. (1907). Ein allgemeiner satz, die bewegung einer reibenden flussigkeit betreffend, nebst einigen anwendungen desselben. *Abhandlungen über theoretische Physik*.

Luo, H. and Pozrikidis, C. (2007). Interception of two spheres with slip surfaces in linear Stokes flow. *Journal of Fluid Mechanics*, 581:129–156.

Luo, H. and Pozrikidis, C. (2008). Effect of surface slip on Stokes flow past a spherical particle in infinite fluid and near a plane wall. *Journal of Engineering Mathematics*, 62(1):1–21.

Maxwell, J. C. (1879). On stresses in rarified gases arising from inequalities of temperature. *Philosophical Transactions of the Royal Society of London*, 170:231–256.

Morawska, L. and Milton, D. K. (2020). It is time to address airborne transmission of covid-19. *Clin Infect Dis*, 6:ciaa939.

Navier, C. L. M. H. (1823). Mémoire sur les lois du mouvement des fluides. *Mémoires de l'Académie Royale des Sciences de l'Institut de France*, 6(1823):389–440.

Nguyen, N.-T. and Wereley, S. T. (2006). *Fundamentals and applications of microfluidics*. Artech House, second edition.

Nieto, C., Power, H., and Giraldo, M. (2012). Boundary element solution of thermal creep flow in microfluidic devices. *Engineering Analysis with Boundary Elements*, 36(7):1062–1073.

Nieto, C., Power, H., and Giraldo, M. (2014). A boundary integral equation formulation for the thermal creep gas flow at finite peclet numbers. *International Journal of Mechanical Sciences*, 88:267–275.

Oberbeck, A. (1876). Ueber stationäre Flüssigkeitsbewegungen mit Berücksichtigung der inneren Reibung. *Journal für die reine und angewandte Mathematik (Crelle's Journal)*, 81:62–80.

Padrino, J. C., Sprittles, J. E., and Lockerby, D. A. (2019). Thermophoresis of a spherical particle: Modelling through moment-based, macroscopic transport equations. *Journal of Fluid Mechanics*, 862:312–347.

Padrino, J. C., Sprittles, J. E., and Lockerby, D. A. (2020). Comment on "Applying a second-kind boundary integral equation for surface tractions in Stokes flow". *Journal of Computational Physics*, 401:109007.

Power, H. and Wrobel, L. C. (1995). *Boundary integral methods in fluid mechanics*. Computational Mechanics Publications.

Pozrikidis, C. (1992). *Boundary integral and singularity methods for linearized viscous flow*. Cambridge University Press.

Ramachandran, A., Tsiglifis, K., and Leal, L. (2012). Properties and solution techniques for a mixed type boundary integral equation arising in creeping flow problems. *Computers & Fluids*, 64:141–156.

Rêgo-Silva, J. J., Power, H., and Wrobel, L. C. (1993). A hypersingular integral equation formulation for Stokes' flow in ducts. *Engineering Analysis with Boundary Elements*, 12(3):185–193.

Rose, W. I., Bluth, G. J., Schneider, D. J., Ernst, G. G., Riley, C. M., Henderson, L. J., and McGimsey, R. G. (2001). Observations of volcanic clouds in their first few days of atmospheric residence: The 1992 eruptions of Crater Peak, Mount Spurr Volcano, Alaska. *The Journal of Geology*, 109(6):677–694.

Rose, W. I. and Durant, A. J. (2009). Fine ash content of explosive eruptions. *Journal of Volcanology and Geothermal Research*, 186(1-2):32–39.

Schwaiger, H. F., Denlinger, R. P., and Mastin, L. G. (2012). Ash3d: A finite-volume, conservative numerical model for ash transport and tephra deposition. *Journal of Geophysical Research*, 117(B04204).

Senchenko, S. and Keh, H. J. (2006). Slipping Stokes flow around a slightly deformed sphere. *Physics of Fluids*, 18(8):088104.

Senchenko, S. and Keh, H. J. (2007). Thermophoresis of a slightly deformed aerosol sphere. *Physics of Fluids*, 19(3):033102.

Settles, G. S. (2006). Fluid mechanics and homeland security. *Annu. Rev. Fluid Mech.*, 38:87–110.

Sharipov, F. (2004). Data on the velocity slip and temperature jump coefficients [gas mass, heat and momentum transfer]. In *Thermal and Mechanical Simulation and Experiments in Microelectronics and Microsystems, 2004. EuroSimE 2004. Proceedings of the 5th International Conference on*, pages 243–249. IEEE.

Sone, Y. (2007). *Molecular gas dynamics: Theory, techniques, and applications*. Springer Science & Business Media.

Struchtrup, H. (2005a). Derivation of 13 moment equations for rarefied gas flow to second order accuracy for arbitrary interaction potentials. *Multiscale Modeling & Simulation*, 3(1):221–243.

Struchtrup, H. (2005b). *Macroscopic transport equations for rarefied gas flows: Approximation methods in kinetic theory*. Springer.

Struchtrup, H., Beckmann, A., Rana, A. S., and Frezzotti, A. (2017). Evaporation boundary conditions for the R13 equations of rarefied gas dynamics. *Physics of Fluids*, 29(9):092004.

Struchtrup, H. and Frezzotti, A. (2016). Evaporation/condensation boundary conditions for the regularized 13 moment equations. In *AIP Conference Proceedings*, volume 1786, page 140002. AIP Publishing.

Struchtrup, H. and Torrilhon, M. (2003). Regularization of Grads 13 moment equations: Derivation and linear analysis. *Physics of Fluids*, 15(9):2668–2680.

Takata, S., Sone, Y., and Aoki, K. (1993). Numerical analysis of a uniform flow of a rarefied gas past a sphere on the basis of the Boltzmann equation for hard-sphere molecules. *Physics of Fluids A: Fluid Dynamics*, 5(3):716–737.

Torrilhon, M. (2010). Slow gas microflow past a sphere: Analytical solution based on moment equations. *Physics of Fluids*, 22(7):072001.

Torrilhon, M. (2016). Modeling nonequilibrium gas flow based on moment equations. *Annual Review of Fluid Mechanics*, 48:429–458.

Torrilhon, M. and Struchtrup, H. (2008). Boundary conditions for regularized 13-moment-equations for micro-channel-flows. *Journal of Computational Physics*, 227(3):1982–2011.

Tyndall, J. (1870). On dust and disease. *Proc. Roy. Instn.*, 6:1–14.

Williams, M. M. R. (1986). Thermophoretic forces acting on a spheroid. *Journal of Physics D: Applied Physics*, 19(9):1631.

Wilson, N., Corbett, S., and Tovey, E. (2020). Airborne transmission of covid-19. *BMJ: British Medical Journal*, 370.

World Health Organization (2003). *Health Aspects of Air Pollution with Particulate Matter, Ozone and Nitrogen Dioxide*. Bonn, Germany. Report on a WHO Working Group, 13-15 January.

Young, J. B. (2011). Thermophoresis of a spherical particle: Reassessment, clarification, and new analysis. *Aerosol Sci. Technol.*, 45(8):927–948.

Youngren, G. and Acrivos, A. (1975). Stokes flow past a particle of arbitrary shape: A numerical method of solution. *Journal of Fluid Mechanics*, 69(2):377–403.